Tahayori, B., H. Meffin, E. N. Sergeev, I. M. Y. Mareels, A. N. Burkitt and D. B. Grayden (2014). Modelling extracellular electrical stimulation: part 4. Effect of the cellular composition of neural tissue on its spatio-temporal filtering properties. Journal of Neural Engineering 11(6): 1-21.

Modeling Extracellular Electrical Stimulation: IV. Effect of the cellular composition of neural tissue on its spatio-temporal filtering properties

Bahman Tahayori[1], Hamish Meffin[1,2], Evgeni N Sergeev[1], Iven MY Mareels[3], Anthony N Burkitt[1,2,4], and David B Grayden[1,2,4]

[1]NeuroEngineering Laboratory, Department of Electrical and Electronic Engineering, The University of Melbourne, VIC 3010, Australia

[2]NICTA Victoria Research Laboratory, VIC 3010, Australia

[3]School of Engineering, The University of Melbourne, VIC 3010, Australia

[4]Bionics Institute, East Melbourne, VIC 3002, Australia

E-mail: bahmant@unimelb.edu.au,hmeffin@unimelb.edu.au

Abstract. *Objective:* The objective of this paper is to present a concrete application of the cellular composite model for calculating the membrane potential, described in an accompanying paper. *Approach:* A composite model that is used to determine the membrane potential for both longitudinal and transverse modes of stimulation is demonstrated. *Main results:* Two extreme limits of the model, near-field and far-field for an electrode close to or distant from a neuron, respectively, are derived in this paper. Results for typical neural tissue are compared using the composite, near-field and far-field models as well as the standard isotropic volume conductor model. The self-consistency of the composite model, its spatial profile response and the extracellular potential time behaviour are presented. The magnitudes of the longitudinal and transverse components for different values of electrode-neurite separations are compared. *Significance:* The unique features of the composite model and its simplified versions can be used to accurately estimate the spatio-temporal response of neural tissue to extracellular electrical stimulation.

1. Introduction

Extracellular electrical stimulation can be used to activate populations of excitable cells in neural tissue. Therefore, it has been used in neuroprosthetic devices to treat neural disorders [1–3]. Applications include: retinal and cochlear implants, deep brain stimulators, pacemakers and prosthetic limbs. Estimating the effect of extracellular electrical stimulation on excitable cells is an important step in designing stimulation strategies for neuroprosthetic devices. Quantitative models, such as volume conductor models in combination with the cable equation, can be used to find the membrane potential of an excitable cell that is induced as a result of an external electric field.

A common approach in modeling extracellular electrical stimulation is based on using a volume conductor model [4, 5]. In volume conductor models, the membrane potential is calculated in two stages. The extracellular electrical potential or current density in the tissue are calculated in Stage 1 through a macroscopic description of neural tissue. The extracellular electric potential (or current density) on the surface of the membrane can be calculated in this stage and is referred to as voltage boundary conditions (or current density boundary conditions). In Stage 2, the membrane potential of the neurite can be calculated using membrane equations available in the literature [6–9]. In Stage 1, it is common to assume that the tissue is isotropic and can be modeled by a single conductivity value [9]. This value is estimated to be about 0.1-0.3 S/m based on experimental data available in the literature [10–12].

Standard volume conductor models consider the tissue to be purely resistive and homogeneous on a microscopic scale. However, tissue is highly heterogeneous on a microscopic scale, comprising both intra- and extracellular spaces, which are separated by a cellular membrane. This causes current to flow in more complicated ways than predicted by a simple resistive volume, because current in the highly confined extracellular spaces will redistribute into the less confined intracellular space by passing across the cellular membrane. Various properties of the membrane make this a non-trivial process, including its high impedance relative to the resistance encountered in either the extra- or intracellular space, its capacitive properties and its elongated spatial extent along neural fibres. As a result the tissue has filtering properties that effect current and voltage distributions on a macroscopic scale spatially (due the length of neurites) and on time scales relevant to neuroprosthetic stimulation. These effects are not captured by standard volume conductors.

A related problem with standard volume conductor approaches is that they contain an internal inconsistency between Stages 1 and 2 of the model [13]. The predicted neural response using standard volume conductor models depends on whether the extracellular voltage or current density around a neurite (from Stage 1) is used as an input to calculate the membrane potential (in Stage 2). Physically this does not make sense, and raises the question of which (if either) prediction is correct.

Intuitively, the mismatch between using the current density or voltage boundary conditions to calculate the membrane potential arises because a two stage model is used

both here and in the literature. The two stages of the model are not consistent with each other because one is essentially solving Maxwell's equations twice; once on the macro-scale in Stage 1 for the tissue and again on the micro-scale in Stage 2 for the neurite. In each case, the solution yields values for the voltage, V_e or current density, J_e, on the boundary of the neurite. These values for both V_e and J_e will be the same for both Stage 1 and Stage 2, if and only if the neurite was embedded in the original Stage 1 volume conductor model. If instead, the neurite is replaced by something else (e.g. an isotropic volume conductor), one can match either V_e or J_e on the boundary of the neurite between Stages 1 and 2, but not both.

The inconsistency associated with standard volume conductor models is a consequence of neglecting the effect of neurites in the tissue on the extracellular voltage and current density in Stage 1. This issue has been addressed in [9,14,15]. Furthermore, such approaches do not account for the effect of neighbouring neurites, which have been shown to be significant. In fact, the problem has its root in the inadequate treatment of the tissue electrical properties as simply resistive, because the specific impedance of the tissue in the Stage 1 volume conductor cannot be matched to the specific impedance of the imbedded neurite in Stage 2. A more technical explanation of the inconsistency of the volume conductor models is given in Appendix A.

In the companion paper [16], we addressed these problems associated with available volume conductor models, by accounting for cellular composition of tissue. We adopted a mean-field theory to provide a mathematical description of the tissue admittivity based on the properties of its cellular constituents. When combined with our previous work on Stage 2 of the volume conductor approach [17, 18], this leads to a class of two-stage cellular composite volume conductor models that is self-consistent (hereafter referred to as the "composite model" for short). The proposed class of models can estimate profiles of electrically evoked neural activity, including phenomena that cannot be predicted by traditional volume conductor models. In this paper, we present results to illustrate how the predictions of this new class of volume conductor models differs from the predictions of standard volume conductors.

1.1. Aims and organisation of this paper

In this paper, we present the analytic solution of the composite model for the simple case of a point source electrode in a bundle of identical parallel fibres. The simplicity of this case allows us to illustrate the distinctive features of the new modelling framework that arise from considering the cellular composition of tissue. We demonstrate how to calculate the extracellular potential, extracellular current density, and membrane potential for the composite model using Fourier techniques. Two standard volume conductor models are derived that approximate the composite model for the near-field and far-field cases. We also consider a standard isotropic volume conductor model. These volume conductor models and the acronyms used for them in this paper are listed in Table 1. We compare the predictions of the composite model to those of the

Table 1. The volume conductor models used in this paper to calculate the membrane potential.

Model	Acronym
Cellular composite volume conductor model	CC
Anisotropic near-field volume conductor model	ANF
Anisotropic far-field volume conductor model	AFF
Isotropic volume conductor model	ISO

three standard models to highlight the differences and similarities.

In the Methods (Section 2), we provide an overview of the composite model for identical parallel fibres and presents how to calculate the extracellular potential or current density using the proposed model. The near-field and far-field approximate models are extracted from the composite model in this section. Equations describing the membrane potential in the Fourier domain are summarised in the same section.

In the Results (Section 3), we demonstrate the distinctive features of the composite model relative to the three standard models: namely its self-consistent prediction of membrane potentials and its spatio-temporal filtering properties that affect the distribution of the extracellular potential, the extracellular current density and the subthreshold membrane potential. At each stage a discussion is provided to interpret the results in terms of the cellular composition of tissue. The discussion also relates the results to previous work and suggests possible implications for neural engineering. In the Discussion (Section 4), the composite model is compared to the available models in the literature. Conclusions of the paper are presented in Section 5.

2. Methods

Consider a piece of neural tissue consisting of parallel fibres in the presence of a point source stimulating electrode as shown in Figure 1. The objective is to calculate the membrane potential of a neurite located at a distance r from the point source. We employ the commonly used two-stage approach. In Stage 1, we use a volume conductor model to calculate the extracellular potential, V_e, or the extracellular current density, $\mathbf{J}_\mathrm{e}$. In Stage 2, we use the equations derived in [17,18] to calculate the longitudinal and transverse components of the membrane potential. These components of membrane potential correspond (respectively) to current passing into and along the neurite in a radially symmetrical fashion, as described by a cable equation, and current passing orthogonally across the neurite, depolarising one side and hyperpolarising the other, as describe by a time-dependent ordinary differential equation. These modes are illustrated in Figure 1 of the companion paper [16].

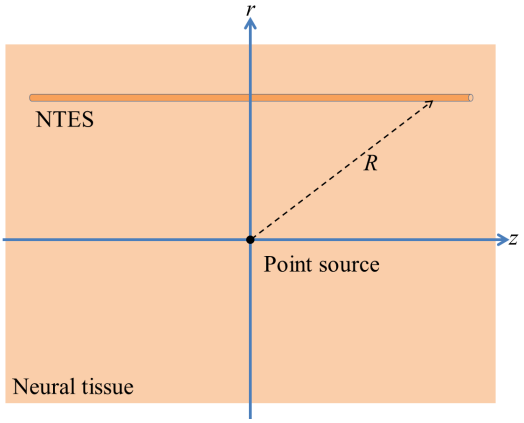

Figure 1. Coordinates setup for a point source.

For Stage 1, four different volume conductor models will be used: the cellular composite model [16], which accounts for the cellular composition of tissue, and three standard volume conductor models corresponding to the near-field and far-field approximations to the composite model and an isotropic model. These are defined further below, but differ from each other in the way the electrical properties of the tissue are modelled through either their admittivity or conductivity.

For Stage 2, in which the results of Stage 1 are used to calculate the subthreshold membrane potential, identical equations will be used for all four models. Consequently difference between predictions of the models are due to the way the tissue properties are captured through either the admittivity or conductivity in Stage 1.

A summary of equations for calculating longitudinal and transverse components of the membrane potential in the Fourier domain, $\hat{\tilde{V}}_{\mathrm{m}}$, as a function of the spatial and temporal Fourier transform of the extracellular current density, $\hat{\tilde{\mathbf{J}}}_{\mathrm{e}}$, or voltage, $\hat{\tilde{V}}_{\mathrm{e}}$ is given in Table 2. The 'L' and 'T' subscripts stand for 'longitudinal' and 'transverse', respectively. Fourier transform notations used throughout are presented in Table 3 and the neurite parameters are given in Table 4. The equations for calculating the longitudinal and transverse components of the extracellular current density and voltage derived in [16] are summarised in Table 5 and are required as inputs for the equations in Table 2. Given that in this paper we only consider the volume conductor model, we have dropped the 'vc' superscript in this paper that was used in [16] to distinguish between volume conductor and bidomain models.

We provide analytic solutions of the membrane potential in the Fourier domain for the composite volume conductor model, anisotropic near-field, anisotropic far-field and isotropic volume conductor models.

Table 2. The membrane potential equations for different modes of stimulation under current density and voltage boundary conditions.

Boundary Conditions	Longitudinal	Transverse
Current Density	$\hat{\tilde{V}}_{\mathrm{m,L}} = \dfrac{2\pi b r_{\mathrm{e}} \lambda_{\mathrm{J}}^2(\omega)}{1 + k_z^2 \lambda_{\mathrm{J}}^2(\omega)} \hat{\tilde{J}}_{\mathrm{e,L}}$	$\hat{\tilde{V}}_{\mathrm{m,T}} = 2R_{\mathrm{e,J}}(1) \hat{\tilde{J}}_{\mathrm{e,T}}$
Voltage	$\hat{\tilde{V}}_{\mathrm{m,L}} = \dfrac{-k_z^2 \lambda_{\mathrm{V}}^2(\omega)}{1 + k_z^2 \lambda_{\mathrm{V}}^2(\omega)} \hat{\tilde{V}}_{\mathrm{e,L}}$	$\hat{\tilde{V}}_{\mathrm{m,T}} = -2\hat{\tilde{V}}_{\mathrm{e,T}}$

Table 3. Fourier transform notations.

Signal	F.T. Notation	F.T. Equation	Inverse F.T. Equation
$f(z)$	$\check{f}(k_z) = \mathcal{F}\{f(z)\}(k_z)$	$\check{f}(k_z) = \dfrac{1}{\sqrt{2\pi}} \displaystyle\int_z f(z) e^{-jk_z z} dz$	$f(z) = \dfrac{1}{\sqrt{2\pi}} \displaystyle\int_{k_z} \check{f}(k_z) e^{jk_z z} dk_z$
$h(t)$	$\hat{h}(\omega) = \mathcal{F}\{h(t)\}(\omega)$	$\hat{h}(\omega) = \dfrac{1}{\sqrt{2\pi}} \displaystyle\int_t h(t) e^{-j\omega t} dt$	$h(t) = \dfrac{1}{\sqrt{2\pi}} \displaystyle\int_\omega \hat{h}(\omega) e^{j\omega t} d\omega$

2.1. Cellular composite model

2.1.1. Stage 1: Calculating the extracellular potential The constitutive and continuity equations in time and space domain are [16]

$$\text{Constitutive Equation:} \qquad \mathbf{J}_{\mathrm{e}} = -\frac{1}{2\pi} \boldsymbol{\xi}_{\mathrm{e}} \underset{z,t}{*} \boldsymbol{\nabla} V_{\mathrm{e}}, \tag{1a}$$

$$\text{Continuity Equation:} \qquad \boldsymbol{\nabla} \cdot \mathbf{J}_{\mathrm{e}} = 0, \tag{1b}$$

where $\mathbf{J}_{\mathrm{e}}$ and V_{e} represent the extracellular current density and voltage, respectively, and $\boldsymbol{\xi}_{\mathrm{e}}$ is the neural tissue admittivity kernel. The above equations in the Fourier domain may be written as

$$\text{Constitutive Equation:} \qquad \hat{\tilde{\mathbf{J}}}_{\mathrm{e}} = -\hat{\tilde{\boldsymbol{\xi}}}_{\mathrm{e}} \check{\boldsymbol{\nabla}} \hat{\tilde{V}}_{\mathrm{e}}, \tag{2a}$$

$$\text{Continuity Equation:} \qquad \check{\boldsymbol{\nabla}} \cdot \hat{\tilde{\mathbf{J}}}_{\mathrm{e}} = 0, \tag{2b}$$

where $\hat{\tilde{\mathbf{J}}}_{\mathrm{e}}$ and $\hat{\tilde{V}}_{\mathrm{e}}$ are Fourier transforms in time and space of the extracellular current density and extracellular potential, respectively. $\check{\boldsymbol{\nabla}} \triangleq [\partial/\partial x, \partial/\partial y, jk_z]$ and

$$\hat{\tilde{\boldsymbol{\xi}}}_{\mathrm{e}}(k_z, \omega) = \begin{bmatrix} \hat{\tilde{\xi}}_{\mathrm{e,T}} & 0 & 0 \\ 0 & \hat{\tilde{\xi}}_{\mathrm{e,T}} & 0 \\ 0 & 0 & \hat{\tilde{\xi}}_{\mathrm{e,L}}(k_z, \omega) \end{bmatrix}, \tag{3}$$

Table 4. Parameters of neural tissue.

Parameter	Description	Unit
a	Neurite radius	m
b	Outer cylinder radius	m
d	Width of the extracellular sheath, $d = b - a$	m
ρ_{i}	Intracellular space resistivity	Ω·m
ρ_{e}	Extracellular space resistivity	Ω·m
r_{i}	Intracellular resistance per unit length, $r_{\mathrm{i}} = \rho_{\mathrm{i}}/\pi a^2$	Ω/m
r_{e}	Extracellular resistance per unit length, $r_{\mathrm{e}} = \rho_{\mathrm{e}}/\pi(b^2 - a^2)$	Ω/m
R_{m}	Membrane's unit area resistance	Ω·m^2
r_{m}	Membrane's unit length resistance, $r_{\mathrm{m}} = R_{\mathrm{m}}/2\pi a$	Ω·m
$R_{\mathrm{e,J}}(1)$	Transverse extracellular specific resistance for current density boundary conditions, $R_{\mathrm{e,J}}(1) = \rho_{\mathrm{e}} b^2/d$	Ω·m^2
C_{m}	Membrane's capacitance per unit area	F/m^2
c_{m}	Membrane's capacitance per unit length, $c_{\mathrm{m}} = 2\pi a C_{\mathrm{m}}$	F/m
τ_{m}	Membrane's time constant, $\tau_{\mathrm{m}} = R_{\mathrm{m}} C_{\mathrm{m}} = r_{\mathrm{m}} c_{\mathrm{m}}$	s
Z_{m}	Membrane's specific impedance, $Z_m = \left(\frac{1}{R_{\mathrm{m}}} + j\omega C_{\mathrm{m}}\right)^{-1}$	Ω·m^2
$\lambda_{0_{\mathrm{J}}}$	Static electrotonic length constant for current density boundary condition, $\lambda_{0_{\mathrm{J}}} = \sqrt{\frac{r_{\mathrm{m}}}{r_{\mathrm{e}} + r_{\mathrm{i}}}}$	m
$\lambda_{\mathrm{J}}(\omega)$	Frequency dependent electrotonic length constant for current density boundary condition, $\lambda_{\mathrm{J}}(\omega) = \frac{\lambda_{0_{\mathrm{J}}}}{\sqrt{1 + j\omega\tau_{\mathrm{m}}}}$	m
$\lambda_{0_{\mathrm{V}}}$	Static electrotonic length constant for voltage boundary condition, $\lambda_{0_{\mathrm{V}}} = \sqrt{\frac{r_{\mathrm{m}}}{r_{\mathrm{i}}}}$	m
$\lambda_{\mathrm{V}}(\omega)$	Frequency dependent electrotonic length constant for voltage boundary condition, $\lambda_{\mathrm{V}}(\omega) = \frac{\lambda_{0_{\mathrm{V}}}}{\sqrt{1 + j\omega\tau_{\mathrm{m}}}}$	m

Table 5. Equations for calculating the longitudinal and transverse components of the current density and voltage boundary condition.

Longitudinal	Transverse
$J_{\mathrm{e,L}}(r,z,t) = -\frac{b}{2}\frac{\partial J_{\mathrm{e},z}(r,z,t)}{\partial z}$	$J_{\mathrm{e,T}}(r,z,t) = -\frac{1}{2}J_{\mathrm{e,r}}(r,z,t)$
$V_{\mathrm{e,L}}(r,z,t) = V_{\mathrm{e}}(r,z,t)$	$V_{\mathrm{e,T}}(r,z,t) = -\frac{b}{2}\frac{\partial V_{\mathrm{e}}(r,z,t)}{\partial r}$

in which

$$\hat{\hat{\xi}}_{\mathrm{e,T}} = \frac{d}{b\rho_{\mathrm{e}}}, \tag{4a}$$

$$\hat{\hat{\xi}}_{\mathrm{e,L}}(k_z,\omega) = \frac{1}{\rho_{\mathrm{i}}}\frac{1+j\omega\tau_m+k_z^2\lambda_{0_{\mathrm{J}}}^2}{1+j\omega\tau_m+k_z^2\lambda_{0_{\mathrm{V}}}^2}. \tag{4b}$$

By substituting the continuity equation into the constitutive equation and transferring the resultant equation into cylindrical coordinates, we obtain

$$\frac{\partial^2\hat{\hat{V}}_{\mathrm{e}}(r,k_z,\omega)}{\partial r^2}+\frac{1}{r}\frac{\partial\hat{\hat{V}}_{\mathrm{e}}(r,k_z,\omega)}{\partial r}-\frac{\hat{\hat{\xi}}_{\mathrm{e,L}}(k_z,\omega)}{\hat{\hat{\xi}}_{\mathrm{e,T}}}\,k_z^2\,\hat{\hat{V}}_{\mathrm{e}}(r,k_z,\omega)=0, \tag{5}$$

where r is the radial distance from the z-axis. The above equation is the modified Bessel's differential equation and the solution is calculated to be

$$\hat{\hat{V}}_{\mathrm{e}}(r,k_z,\omega)=\frac{\hat{I}(\omega)}{4\pi\hat{\hat{\xi}}_{\mathrm{e,T}}}\sqrt{\frac{2}{\pi}}K_0\Big(\hat{\hat{\chi}}(k_z,\omega)\,r|k_z|\Big), \tag{6}$$

where $\hat{\hat{\chi}}(k_z,\omega)$ is a measure of anisotropy and is defined to be

$$\hat{\hat{\chi}}(k_z,\omega)\triangleq\sqrt{\frac{\hat{\hat{\xi}}_{\mathrm{e,L}}(k_z,\omega)}{\hat{\hat{\xi}}_{\mathrm{e,T}}}}. \tag{7}$$

In Equation (6), $\hat{I}(\omega)$ is the time Fourier transform of the applied current through the point source and K_0 represents the zeroth order modified Bessel's function of the second kind. The details of deriving Equation (5) and calculating its solution are presented in Appendix B. The current density in the time and space Fourier domain can also be calculated from the constitutive equation, which results in

$$\begin{aligned}\hat{\hat{\mathbf{J}}}_{\mathrm{e}}(r,k_z,\omega)=\frac{\hat{I}(\omega)}{4\pi}\sqrt{\frac{2}{\pi}}\Big(&\hat{\hat{\chi}}(k_z,\omega)|k_z|K_1\left(\hat{\hat{\chi}}(k_z,\omega)r|k_z|\right)\mathbf{e}_r\\&-jk_z\,\hat{\hat{\chi}}^2(k_z,\omega)K_0\left(\hat{\hat{\chi}}(k_z,\omega)r|k_z|\right)\mathbf{e}_z\Big),\end{aligned} \tag{8}$$

where $\mathbf{e}_r$ and $\mathbf{e}_z$ are unit vectors in the radial and z-directions, respectively. In the above equation, K_1 is the first-order modified Bessel's function of the second kind. A summary of the equations describing the extracellular current density and voltage in the tissue is presented in Table 6.

2.1.2. Stage 2: Calculating the membrane potential The membrane potential in the Fourier domain can be calculated for both longitudinal and transverse modes of stimulation using equations presented in Tables 2 and 5. Therefore, the longitudinal

and transverse membrane potential in the time and space Fourier domain, either using voltage or current density boundary conditions, can be written as‡

$$\hat{\tilde{V}}_{\mathrm{m,L}} = -\frac{k_z^2 \lambda_V^2(\omega)\hat{I}(\omega)}{4\pi\hat{\tilde{\xi}}_{\mathrm{e,T}}\Big(1+k_z^2\lambda_V^2(\omega)\Big)}\sqrt{\frac{2}{\pi}}K_0\Big(\hat{\tilde{\chi}}(k_z,\omega)r|k_z|\Big), \tag{9a}$$

$$\hat{\tilde{V}}_{\mathrm{m,T}} = \frac{b\hat{I}(\omega)\hat{\tilde{\chi}}(k_z,\omega)|k_z|}{4\pi\hat{\tilde{\xi}}_{\mathrm{e,T}}}\sqrt{\frac{2}{\pi}}K_1\Big(\hat{\tilde{\chi}}(k_z,\omega)r|k_z|\Big)\cos\theta, \tag{9b}$$

in which θ is the azimuth angle in cylindrical coordinates on the surface of the cylindrical neurite, with respect to a reference line from the centre of the cylinder to the point source at the origin. The membrane potential in the Fourier domain for the longitudinal and transverse components are also presented in Table 7. For the cellular composite model, $\chi^{\mathrm{mdl}} = \hat{\tilde{\chi}}(k_z,\omega)$ and $\xi_{\mathrm{e,T}}^{\mathrm{mdl}} = \hat{\tilde{\xi}}_{\mathrm{e,T}}$.

To find the longitudinal and transverse components of the membrane potential, we apply the two-dimensional inverse Fourier transform in both space and time. The overall membrane potential of a neurite as a function of its distance from the point source stimulating electrode, r, is

$$V_{\mathrm{m}}(r,z,\theta,t) = V_{\mathrm{m,L}}(r,z,t) + V_{\mathrm{m,T}}(r,z,\theta,t). \tag{10}$$

2.2. Anisotropic near-field model

For a standard anisotropic volume conductor model of tissue, the constitutive and the continuity equations can be written as

$$\text{Constitutive Equation:} \qquad \mathbf{J}_{\mathrm{e}} = -\sigma^{\mathrm{mdl}}\boldsymbol{\nabla}V_{\mathrm{e}}, \tag{11a}$$

$$\text{Continuity Equation:} \qquad \boldsymbol{\nabla}\cdot\mathbf{J}_{\mathrm{e}} = 0, \tag{11b}$$

where $\mathbf{J}_{\mathrm{e}}$ and V_{e} are extracellular current density and voltage, respectively, and σ^{mdl} represents the model conductivity tensor,

$$\sigma^{\mathrm{mdl}} = \begin{bmatrix} \sigma_{\mathrm{e,T}}^{\mathrm{mdl}} & 0 & 0 \\ 0 & \sigma_{\mathrm{e,T}}^{\mathrm{mdl}} & 0 \\ 0 & 0 & \sigma_{\mathrm{e,L}}^{\mathrm{mdl}} \end{bmatrix}, \tag{12}$$

in which $\sigma_{\mathrm{e,L}}^{\mathrm{mdl}}$ and $\sigma_{\mathrm{e,T}}^{\mathrm{mdl}}$ are conductivities in the longitudinal and transverse directions, respectively. When the stimulating electrode is sufficiently close to the neurite, which is referred to as the near-field, we show in Appendix C that small values of r and z corresponds to large values of k_z. Therefore, the longitudinal and the transverse

‡ Given that $Z_{\mathrm{m}} \gg R_{\mathrm{i,V}}(1), R_{\mathrm{e,V}}(1)$, the full version expression for the longitudinal membrane potential, $\hat{\tilde{V}}_{\mathrm{m,T}} = \frac{1}{\sqrt{2\pi}}\left(\frac{Z_{\mathrm{m}}b}{Z_{\mathrm{m}}+R_{\mathrm{i,V}}(1)+R_{\mathrm{e,V}}(1)}\right)\frac{\hat{I}(\omega)\hat{\tilde{\chi}}(k_z,\omega)|k_z|}{4\pi\hat{\tilde{\xi}}_{\mathrm{e,T}}}K_1\Big(\hat{\tilde{\chi}}(k_z,\omega)r|k_z|\Big)\cos\theta$, simplifies to Equation (9b). More explanation is given in [16].

Table 6. Extracellular voltage and current density in time-space domain and the Fourier domain for the composite and standard models used in this paper. $\xi_{\mathrm{e,T}}^{\mathrm{mdl}}$ and χ^{mdl} for each model are given in Table 8.

Fourier Domain	Time-Space Domain
Composite	
$\hat{\tilde{V}}_{\mathrm{e}} = \dfrac{\hat{I}(\omega)}{4\pi\hat{\tilde{\xi}}_{\mathrm{e,T}}}\sqrt{\dfrac{2}{\pi}}K_0\Big(\hat{\tilde{\chi}}(k_z,\omega)\, r\lvert k_z\rvert\Big)$	$V_{\mathrm{e}} = DFT^{-1}\{\hat{\tilde{V}}_{\mathrm{e}}\}$
$\hat{\tilde{\mathbf{J}}}_{\mathrm{e}} = \dfrac{\hat{I}(\omega)}{4\pi}\sqrt{\dfrac{2}{\pi}}\hat{\tilde{\chi}}(k_z,\omega)\Big(\lvert k_z\rvert K_1\big(\hat{\tilde{\chi}}(k_z,\omega) r\lvert k_z\rvert\big)\mathbf{e}_r - jk_z\,\hat{\tilde{\chi}}(k_z,\omega)K_0\big(\hat{\tilde{\chi}}(k_z,\omega) r\lvert k_z\rvert\big)\mathbf{e}_z\Big)$	$\mathbf{J}_{\mathrm{e}} = DFT^{-1}\{\hat{\tilde{\mathbf{J}}}_{\mathrm{e}}\}$
Standard models (near-field, far-field and isotropic)	
$\hat{\tilde{V}}_{\mathrm{e}} = \dfrac{\hat{I}(\omega)}{4\pi\sigma_{\mathrm{e,T}}^{\mathrm{mdl}}}\sqrt{\dfrac{2}{\pi}}K_0\left(\chi^{\mathrm{mdl}} r\lvert k_z\rvert\right)$	$V_{\mathrm{e}} = \dfrac{I(t)}{4\pi\sigma_{\mathrm{e,T}}^{\mathrm{mdl}}\sqrt{(\chi^{\mathrm{mdl}})^2 r^2 + z^2}}$
$\hat{\tilde{\mathbf{J}}}_{\mathrm{e}} = \dfrac{\hat{I}(\omega)}{4\pi}\sqrt{\dfrac{2}{\pi}}\chi^{\mathrm{mdl}}\Big(\lvert k_z\rvert K_1\left(\chi^{\mathrm{mdl}} r\lvert k_z\rvert\right)\mathbf{e}_r - jk_z\,\chi^{\mathrm{mdl}}K_0\left(\chi^{\mathrm{mdl}} r\lvert k_z\rvert\right)\mathbf{e}_z\Big)$	$\mathbf{J}_{\mathrm{e}} = \dfrac{I(t)\left((\chi^{\mathrm{mdl}})^2 r\mathbf{e}_r + z\mathbf{e}_z\right)}{4\pi\left((\chi^{\mathrm{mdl}})^2 r^2 + z^2\right)^{3/2}}$

Table 7. Equations for the membrane potential under voltage and current density boundary conditions. $\xi_{\mathrm{e,T}}^{\mathrm{mdl}}$ and χ^{mdl} for each model are given in Table 8.

	Voltage boundary condition
Longitudinal	$\hat{\tilde{V}}_{\mathrm{m,L}}(r,k_z,\omega) = -\dfrac{k_z^2\lambda_V^2(\omega)\hat{I}(\omega)}{4\pi\xi_{\mathrm{e,T}}^{\mathrm{mdl}}\Big(1+k_z^2\lambda_V^2(\omega)\Big)}\sqrt{\dfrac{2}{\pi}}K_0\Big(\chi^{\mathrm{mdl}} r\lvert k_z\rvert\Big)$
Transverse	$\hat{\tilde{V}}_{\mathrm{m,T}}(r,k_z,\theta,\omega) = \dfrac{b\chi^{\mathrm{mdl}}\hat{I}(\omega)}{4\pi\xi_{\mathrm{e,T}}^{\mathrm{mdl}}}\sqrt{\dfrac{2}{\pi}}k_z K_1\Big(\chi^{\mathrm{mdl}} r\lvert k_z\rvert\Big)\cos\theta$
	Current density boundary condition
Longitudinal	$\hat{\tilde{V}}_{\mathrm{m,L}}(r,k_z,\omega) = \dfrac{-b^2k_z^2\lambda_{\mathrm{J}}^2(\omega)\left(\chi^{\mathrm{mdl}}\right)^2 r_{\mathrm{e}}\hat{I}(\omega)}{4\Big(1+k_z^2\lambda_{\mathrm{J}}^2(\omega)\Big)}\sqrt{\dfrac{2}{\pi}}K_0\Big(\chi^{\mathrm{mdl}} r\lvert k_z\rvert\Big)$
Transverse	$\hat{\tilde{V}}_{\mathrm{m,T}}(r,k_z,\theta,\omega) = \dfrac{R_{\mathrm{e,J}}(1)\chi^{\mathrm{mdl}}\hat{I}(\omega)}{4\pi}\sqrt{\dfrac{2}{\pi}}k_z K_1\Big(\chi^{\mathrm{mdl}} r\lvert k_z\rvert\Big)\cos\theta$

components of the conductivity can be calculated from Equation (4) as $k_z \to \infty$. Thus, for the near-field model,

$$\sigma_{\mathrm{e,L}}^{\mathrm{ANF}} = \lim_{k_z \to \infty} \xi_{\mathrm{e,L}}(k_z, \omega) = \frac{2d}{b\rho_{\mathrm{e}}}, \tag{13a}$$

$$\sigma_{\mathrm{e,T}}^{\mathrm{ANF}} = \xi_{\mathrm{e,T}} = \frac{d}{b\rho_{\mathrm{e}}}. \tag{13b}$$

In this case, the extracellular voltage in the Fourier domain is

$$\hat{\tilde{V}}_{\mathrm{e}}(r, k_z, \omega) = \frac{\hat{I}(\omega)}{4\pi\sigma_{\mathrm{e,T}}^{\mathrm{ANF}}} \sqrt{\frac{2}{\pi}} K_0\left(\chi^{\mathrm{ANF}} r |k_z|\right) \tag{14}$$

where

$$\chi^{\mathrm{ANF}} \triangleq \sqrt{\frac{\sigma_{\mathrm{e,L}}^{\mathrm{ANF}}}{\sigma_{\mathrm{e,T}}^{\mathrm{ANF}}}} = \sqrt{2}. \tag{15}$$

Equation (14) can be inverted analytically to give the extracellular potential in the time-space domain. The analytic results are given in Table 6. The membrane potential for both modes of stimulation can be calculated from equations given in Table 7 by setting $\chi^{\mathrm{mdl}} = \chi^{\mathrm{ANF}}$ and $\xi_{\mathrm{e,T}}^{\mathrm{mdl}} = \sigma_{\mathrm{e,T}}^{\mathrm{ANF}}$.

2.3. Anisotropic far-field model

We show in Appendix C that the far-field corresponds to small values of k_z. The constitutive and the continuity equation indicated by Equation (11) apply in this case as well. In the far-field limit, the longitudinal and the transverse components of the conductivity can be calculated from Equation (4),

$$\sigma_{\mathrm{e,L}}^{\mathrm{AFF}} = \lim_{k_z \to 0} \xi_{\mathrm{e,L}}(k_z, \omega) = \frac{1}{\rho_{\mathrm{i}}}, \tag{16a}$$

$$\sigma_{\mathrm{e,T}}^{\mathrm{AFF}} = \xi_{\mathrm{e,T}} = \frac{d}{b\rho_{\mathrm{e}}}. \tag{16b}$$

The extracellular potential in the Fourier domain is

$$\hat{\tilde{V}}_{\mathrm{e}}(r, k_z, \omega) = \frac{\hat{I}(\omega)}{4\pi\sigma_{\mathrm{e,T}}^{\mathrm{AFF}}} \sqrt{\frac{2}{\pi}} K_0\left(\chi^{\mathrm{AFF}} r |k_z|\right) \tag{17}$$

where

$$\chi^{\mathrm{AFF}} \triangleq \sqrt{\frac{\sigma_{\mathrm{e,L}}^{\mathrm{AFF}}}{\sigma_{\mathrm{e,T}}^{\mathrm{AFF}}}} = \sqrt{\frac{b\rho_{\mathrm{e}}}{d\rho_{\mathrm{i}}}}. \tag{18}$$

The extracellular voltage and current density in the time-space domain can also be calculated analytically and the results are presented in Table 6. Similar to the near-field model, the membrane potential for both modes of stimulation can be calculated from equations given in Table 7 by setting $\chi^{\mathrm{mdl}} = \chi^{\mathrm{AFF}}$ and $\xi_{\mathrm{e,T}}^{\mathrm{mdl}} = \sigma_{\mathrm{e,T}}^{\mathrm{AFF}}$.

2.4. Standard isotropic volume conductor model

In an isotropic volume conductor model, the neural tissue conductivity is direction independent. Therefore, $\sigma_{\mathrm{e,T}}^{\mathrm{ISO}} = \sigma_{\mathrm{e,L}}^{\mathrm{ISO}} = \sigma_0$ where σ_0 is a constant. In this case, $\chi^{\mathrm{ISO}} = 1$. As a result, in Equation (11a), the conductivity of tissue, σ^{mdl}, can be modeled by a single scalar, σ_0.

The extracellular voltage and current density at an arbitrary point at distance R from the point source stimulating electrode shown in Figure 1 are calculated to be

$$V_{\mathrm{e}} = \frac{I}{4\pi\sigma_0 R} = \frac{I}{4\pi\sigma_0\sqrt{r^2+z^2}}, \tag{19a}$$

$$\mathbf{J}_{\mathrm{e}} = \frac{I}{4\pi R^2}\mathbf{e}_R = \frac{I}{4\pi(r^2+z^2)^{3/2}}(r\mathbf{e}_r + z\mathbf{e}_z), \tag{19b}$$

where $\mathbf{e}_R$ is the unit vector in the radial direction in spherical coordinates and $\mathbf{e}_r$ and $\mathbf{e}_z$ are unit vectors in the radial direction and the z-direction in cylindrical coordinates. The extracellular voltage and current density in the time-space domain and the Fourier domain are presented in Table 6.

The longitudinal and the transverse components of the membrane potential can be calculated from the equations presented in Table 7 by setting $\chi^{\mathrm{mdl}} = \chi^{\mathrm{ISO}} = 1$ and $\xi_{\mathrm{e,T}}^{\mathrm{mdl}} = \sigma_{\mathrm{e,T}}^{\mathrm{ISO}} = \sigma_0$.

A summary of admittivities and conductivities in the longitudinal and transverse directions for the four models described in this section is presented in Table 8. The square root of the ratio of the longitudinal to the transverse component of the admittivity for each model, χ^{mdl}, is presented in the table as well.

3. Results

In this section, we compare the results of numerical calculations in MATLAB for the four volume conductor models introduced in Section 2:

(i) The composite model whose admittivity kernel is given by Equations (3) and (4);

(ii) The near-field model with $\sigma_{\mathrm{e,L}} = 1/\rho_{\mathrm{i}}$ and $\sigma_{\mathrm{e,T}} = \dfrac{d}{b\rho_{\mathrm{e}}}$;

(iii) The far-field model with $\sigma_{\mathrm{e,L}} = \dfrac{2d}{b\rho_{\mathrm{e}}}$ and $\sigma_{\mathrm{e,T}} = \dfrac{d}{b\rho_{\mathrm{e}}}$;

(iv) The standard isotropic model with $\sigma_0 = 0.1\mathrm{S/m}$.

It should be noted that the near-field, far-field and the isotropic models are standard volume conductor models that do not account for the electrical properties of the tissue due to its cellular composition. The only model that considers these properties of the tissue is the composite model.

We present the results in three different categories to emphasise the differences between the composite model and the three standard volume conductor models. First, we demonstrate that the composite model gives self-consistent answers for the membrane

Table 8. Admittivities and conductivities in the longitudinal and transverse directions for the models described in Section 2. Note that for the composite model, the admittivity is presented while for other models conductivities are presented. The expressions in this table can be used to calculate the membrane potential for longitudinal and transverse modes of stimulation under voltage and current density boundary conditions presented in Table 7.

Model	Longitudinal ($\xi_{\mathrm{e,L}}^{\mathrm{mdl}}$)	Transverse ($\xi_{\mathrm{e,T}}^{\mathrm{mdl}}$)	χ^{mdl}
Composite	$\hat{\xi}_{\mathrm{e,L}}(k_z,\omega)=\frac{1}{\rho_{\mathrm{i}}}\frac{1+k_z^2\lambda_{\mathrm{J}}^2(\omega)}{1+k_z^2\lambda_{\mathrm{V}}^2(\omega)}$	$\hat{\xi}_{\mathrm{e,T}}=\frac{d}{b\rho_{\mathrm{e}}}$	$\hat{\chi}(k_z,\omega)\triangleq\sqrt{\frac{\hat{\xi}_{\mathrm{e,L}}(k_z,\omega)}{\hat{\xi}_{\mathrm{e,T}}}}$
Near-field	$\sigma_{\mathrm{e,L}}^{\mathrm{ANF}}=\frac{2d}{b\rho_{\mathrm{e}}}$	$\sigma_{\mathrm{e,T}}^{\mathrm{ANF}}=\frac{d}{b\rho_{\mathrm{e}}}$	$\chi^{\mathrm{ANF}}\triangleq\sqrt{\frac{\sigma_{\mathrm{e,L}}^{\mathrm{ANF}}}{\sigma_{\mathrm{e,T}}^{\mathrm{ANF}}}}=\sqrt{2}$
Far-field	$\sigma_{\mathrm{e,L}}^{\mathrm{AFF}}=\frac{1}{\rho_{\mathrm{i}}}$	$\sigma_{\mathrm{e,T}}^{\mathrm{AFF}}=\frac{d}{b\rho_{\mathrm{e}}}$	$\chi^{\mathrm{AFF}}\triangleq\sqrt{\frac{\sigma_{\mathrm{e,L}}^{\mathrm{AFF}}}{\sigma_{\mathrm{e,T}}^{\mathrm{AFF}}}}=\sqrt{\frac{b\rho_{\mathrm{e}}}{d\rho_{\mathrm{i}}}}$
Isotropic	$\sigma_{\mathrm{e,L}}^{\mathrm{ISO}}=\sigma_0$	$\sigma_{\mathrm{e,T}}^{\mathrm{ISO}}=\sigma_0$	$\chi^{\mathrm{ISO}}\triangleq\sqrt{\frac{\sigma_{\mathrm{e,L}}^{\mathrm{ISO}}}{\sigma_{\mathrm{e,T}}^{\mathrm{ISO}}}}=1$

Table 9. Parameters of the neurite used in simulations. These are nominal values taken from literature [19–32].

b(m)	d(m)	$\rho_{\mathrm{i}}(\Omega\cdot\mathrm{m})$	$\rho_{\mathrm{e}}(\Omega\cdot\mathrm{m})$	$R_{\mathrm{m}}(\Omega\cdot\mathrm{m}^2)$	$C_{\mathrm{m}}(\mathrm{F/m}^2)$
0.5×10^{-6}	0.03×10^{-6}	0.7	0.7	1	0.01

potential, independent of boundary condition type in Stage 2, whereas the standard models do not. Second, we examine the spatial profile of the composite model and demonstrate that it interpolates between the two extreme cases of the near-field and the far-field models. The contribution of the longitudinal and transverse modes of stimulation to the overall membrane potential in the composite model are presented. Finally, the temporal behaviour of all models are compared.

The parameters of neural tissue used throughout are presented in Table 9 and are nominal values taken from the literature [19–32]. The parameters of the neurite derived from these parameters are presented in Table 10. Except where noted otherwise, simulations are performed for a cathodic first, biphasic pulse stimulus with 1μA amplitude and pulse duration of $\tau_p = 100\mu$s per phase. We present the results for the longitudinal component of the membrane potential, $V_{\mathrm{m,L}}$, followed by the results for the transverse component of the membrane potential, $V_{\mathrm{m,T}}$.

Table 10. Calculated parameters of the neurite.

τ_{m}(s)	r_{m}(Ω·m)	r_{i}(Ω/m)	r_{e}(Ω/m)	$\lambda_{0_{\mathrm{J}}}$(m)	$\lambda_{0_{\mathrm{V}}}$(m)
1×10^{-2}	3.39×10^{5}	1×10^{12}	7.66×10^{12}	1.98×10^{-4}	5.79×10^{-4}

3.1. The composite model gives a self-consistent membrane potential but the standard models do not

3.1.1. Longitudinal mode of stimulation Figure 2 provides an example of the cylinder plots of the longitudinal component of the membrane potential for the composite, near-field, far-field and isotropic models at the end of the cathodic phase (first phase) of the stimulation, $t = 100\mu$s. In this example, the electrode-neurite separation is set to $r = 50\mu$m. The top row in each part of this figure represents the (longitudinal) membrane potential under voltage boundary conditions while the bottom row in each part represents the (longitudinal) membrane potential under current density boundary conditions. The same color-map is used for all plots in this figure. These plots illustrate that only the composite model results in a self-consistent membrane potential that is the same across boundary conditions types.

The axial symmetry feature of the longitudinal component is clearly demonstrated in Figure 2. It can be observed from these plots that the maximum depolarisation occurs at $z = 0$, which is located under the point source stimulating electrode. Furthermore, all models predict a symmetric hyperpolarising effect at some distance from $z = 0$. The magnitude and spatial extent of polarisation depends not only on the type of the model, but also on the type of the boundary condition applied for all models except the composite model. The greatest level of discrepancy is present in the isotropic volume conductor model, both in terms of magnitude and spatial extent of polarisation.

A quantitative comparison of the longitudinal component of the membrane potential predicted by these models is presented in Figure 3 for a range of electrode-neurite separations, r. The longitudinal membrane potential directly under the electrode, $z = 0$, at the end of the cathodic phase ($t = 100\mu$s) is plotted for each model under voltage and current density boundary conditions. This figure emphasises the fact that the only self-consistent model is the composite model. The near-field and far-field models are self-consistent for small and large electrode-neurite separations, respectively. For the isotropic model, the discrepancy between current density and voltage boundary conditions exists across the whole electrode-neurite separation range. Discrepancies for all three standard models can range up to nearly an order of magnitude over the range of r examined.

3.1.2. Transverse mode of stimulation

For the same neurite in Section 3.1.1, the cylindrical plot of the transverse

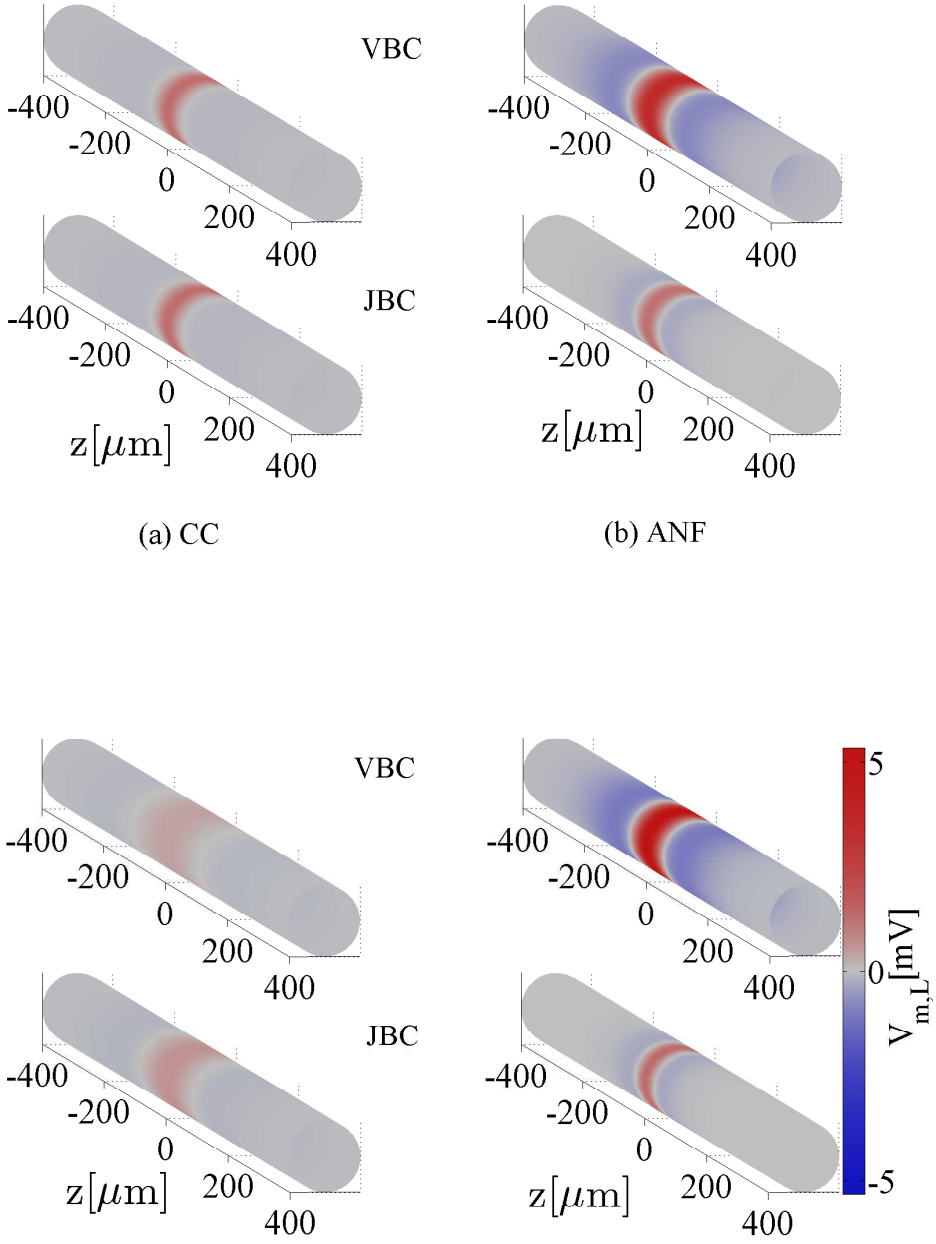

(a) CC (b) ANF

(c) AFF (d) ISO

Figure 2. The longitudinal component of the membrane potential at the end of the cathodic phase, $V_{\mathrm{m,L}}(z, t = \tau_p)$, for voltage and current density boundary conditions for the neurite whose parameters are presented in Table 9. Comparison is made for (a) composite, (b) near-field, (c) far-field and (d) isotropic models. The top row on each figure represents the membrane potential under voltage boundary conditions (VBC) and the bottom row represents the result for the current density boundary conditions (JBC). The red color represents depolarisation while the blue represents the hyperpolarisation effect. For the isotropic model, a typical value of σ_0 is considered for the tissue conductivity. The electrode-neurite separation is $r = 50\mu$m.

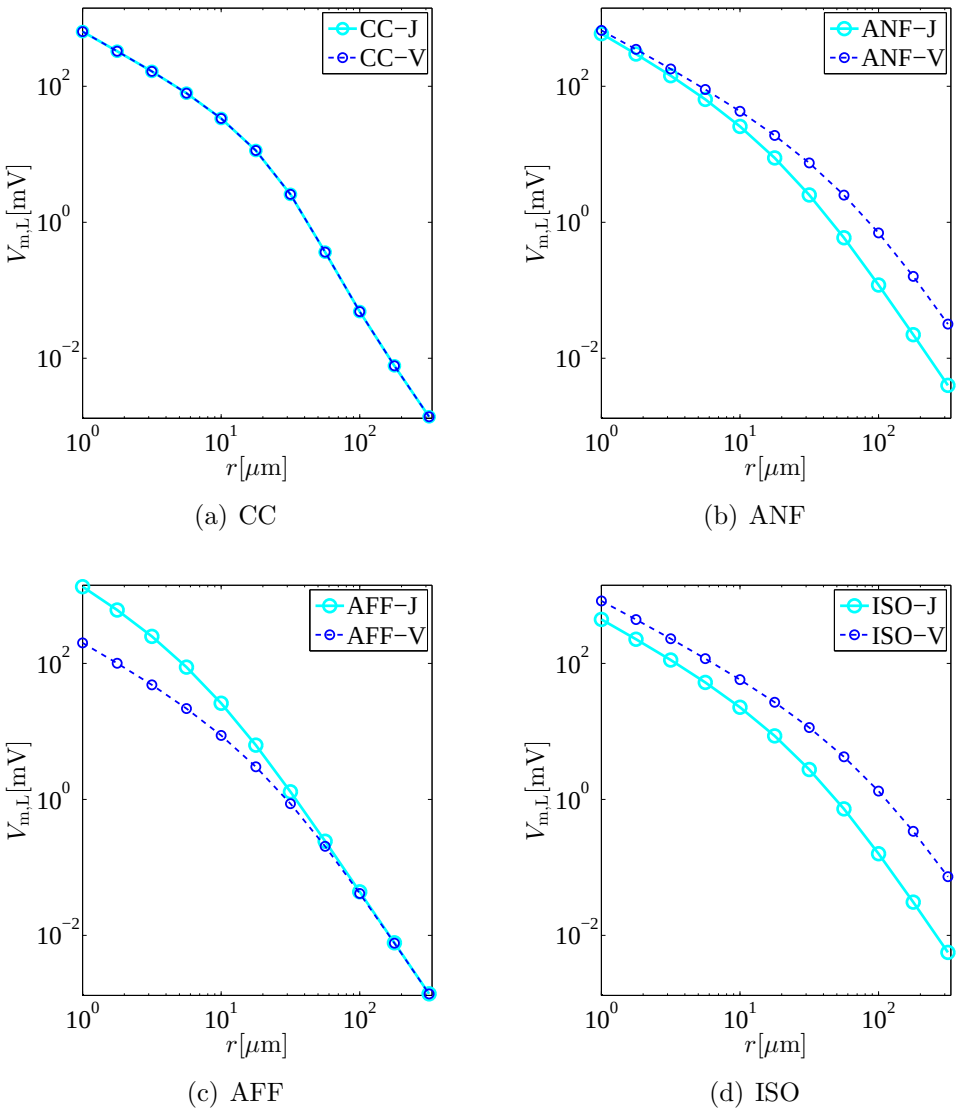

(a) CC (b) ANF

(c) AFF (d) ISO

Figure 3. The maximum depolarisation generated by the longitudinal component of the membrane potential at the end of the cathodic phase, $V_{\mathrm{m,L}}(z = 0, t = \tau_p)$, under voltage and current density boundary conditions as a function of the electrode-neurite separation, r. Simulation results compare the four models described in this paper, (a) composite, (b) near-field, (c) far-field and (d) isotropic.

component of the membrane potential under a point source stimulation with the same biphasic profile is shown in Figure 4. The format of this figure is the same as of Figure 2.

Figure 4 illustrates the qualitative differences between the transverse and longitudinal modes of the membrane potential when compared to the plot presented in Figure 2. There is no axial symmetry in the transverse mode of stimulation and at each point in time, opposite sides of the fibre are depolarised and hyperpolarised with the same magnitude of potential. The maximum depolarisation in the transverse mode occurs at $z = 0$ and an angle $\theta = 0$ corresponding to the side of the neurite directly facing the electrode.

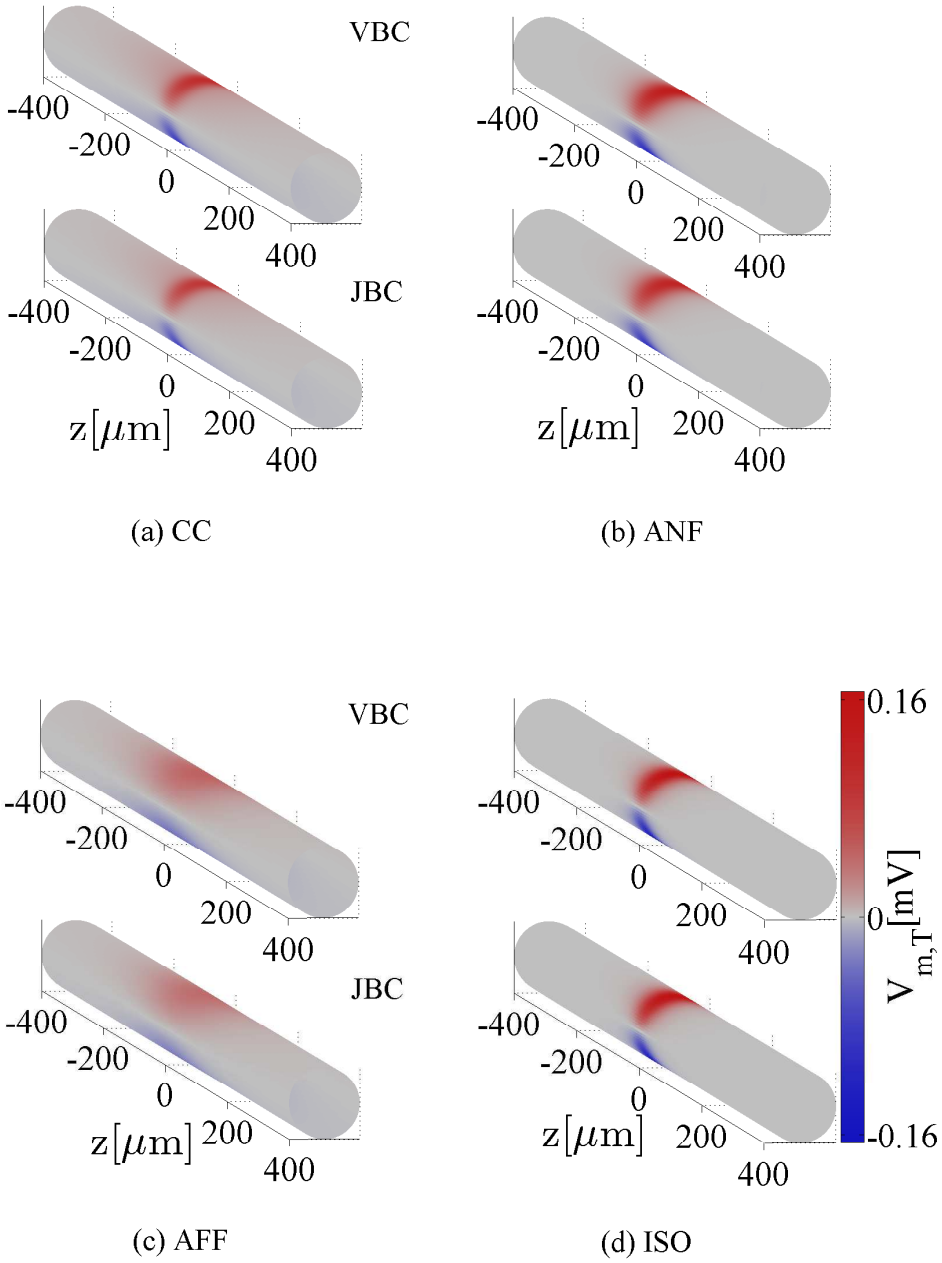

Figure 4. The transverse component of the membrane potential at the end of the cathodic phase, $V_{\mathrm{m,L}}(z, t = \tau_p)$, for voltage and current density boundary conditions for the neurite whose parameters are presented in Table 9. Comparison is made for (a) composite, (b) near-field, (c) far-field and (d) isotropic models. The electrode-neurite separation is $r = 50\mu$m. The figure format is the same as of Figure 2.

It can be shown that the transverse mode of the membrane potential is self-consistent, not only for the composite model, but also for the near-field and far-field models (see equations in Table 7 for $\hat{\hat{V}}_{\mathrm{m,T}}$; notice that the ratio between voltage and current density boundary conditions is unity). This is evident in Figure 4. For the isotropic model, the predicted values of the membrane potential are not self-consistent, but differ by a constant factor (equal to 6/7 for the parameters used here).

3.1.3. Discussion of the results In contrast to standard models, the composite model connects the microscopic properties of the neurite in Stage 2 to the macroscopic electrical properties of the tissue in Stage 1 by introducing a non-local and non-instantaneous anisotropic admittivity kernel for the neural tissue. In particular, self-consistency across the two stages in the composite model is guaranteed, by ensuring that V_{e} and $\mathbf{J}_{\mathrm{e}}$ from the Stage 1 volume conductor satisfy the transimpedance equation for an individual neurite derived in [17] on the neurites boundaries. Therefore, the membrane potential calculated through the composite model results in a self-consistent membrane potential, regardless of whether V_{e} or $\mathbf{J}_{\mathrm{e}}$ is applied as a boundary condition in Stage 2. By contrast, the transimpedance of a cylindrical volume corresponding to a neurite in a standard volume conductor model is not matched to that of an actual neurite, so that inconsistency results.

It should be noted that choosing V_{e} as a boundary conditions in standard models (which is standard practice in two-stage volume conductor models) does not provide a generally better approximation to the predictions of the composite model than does choosing $\mathbf{J}_{\mathrm{e}}$ as a boundary condition (see Figure 3). While it is possible to find a standard volume conductor model that approximates the composite model's predictions for a limited range of electrode-neurite separations (e.g., far-field or near-field models), it is not possible to find a standard model that well approximates the composite model over the whole range. Thus fitting or applying standard models to data over a wide range of electrode-neurite separations is expected to result in errors in some parts of the range, which can be in excess of several hundred percent.

3.2. The membrane potential of the composite model differs in spatial profile and magnitude compared to standard models: Interpolating between near and far field models

3.2.1. Extracellular potential The extracellular potential in the tissue, V_{e}, gives rise to the driving term in the neurite equations presented in Table 2. These neurite equations are the same for all four models. Therefore, differences in the spatial pattern of membrane potential arise because of differences in the extracellular potential distribution across the tissue. To inspect the spatial behaviour of each model described in Section 2, we plot V_{e} along the fibre (z direction) as a function of the electrode-neurite separation for each model. The results at the end of the first (cathodic) phase of the stimulus ($t = 100\mu$s) are presented in Figure 5. Both z and r range logarithmically from

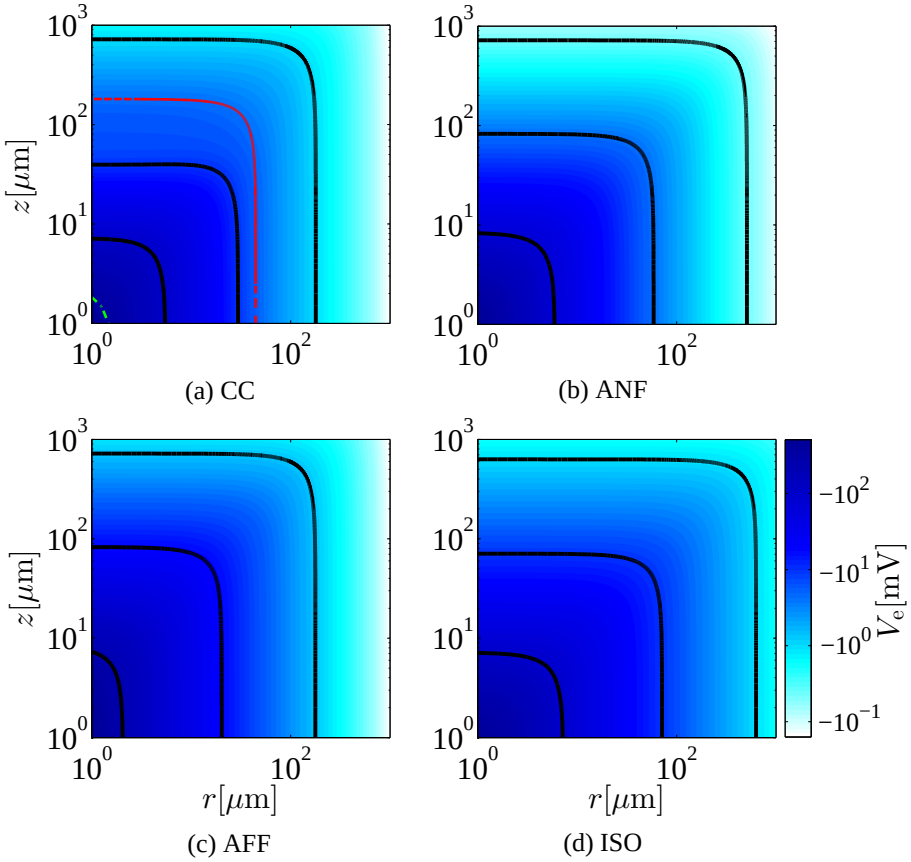

Figure 5. The extracellular potential in neural tissue, V_e, parallel to fibres as a function of electrode-neurite separation, r, at $t = \tau_p$ (see Figure 1 for description of r and z). V_e is calculated for a point source for (a) the composite model, (b) the near-field model, (c) the far-field model and (d) the isotropic model. The black solid lines represent equipotential lines for three voltage levels, 1mV, 10mV and 100mV, for each model. The red dashed line represent the equipotential line generated by the far-field model with 5% error compared to the composite model. The green dash-dotted line is the equipotential line generated by the near-field model with 5% error compared to the composite model.

1μm to 1mm. It should be noted that as the electrode-neurite separation, r, and the distance from the centre of the neurite increase, the extracellular potential decreases dramatically. Therefore, in order to be able to show the membrane potential along the fibre as a function of the electrode-neurite separation, logarithmic scales are used. The black solid lines represent equipotential lines for three voltage levels, 1mV, 10mV and 100mV, for each model. The red dashed line represent the equipotential line generated by the far-field model with 5% error compared to the composite model. Therefore, for any far-field larger than what is marked by this line, the error of the far-field model is less than 5%. The green dash-dotted line is the equipotential line generated by the near-field model with 5% error compared to the composite model. Thus, if the electrode-neurite separations is smaller than what is marked by this line, the error of the near-field model is within 5% compared to the composite model.

Plots in Figure 5 clearly show the difference between the spatial profile created by the composite model and the other models. Figure 5(a) shows the intrinsic anisotropy of the composite model. For small values of r and z, the extracellular potential predicted by the near-field model converges to the composite model as shown in Figure 5(b). In the far-field limit, the extracellular potential predicted by the far-field model approaches the composite model as illustrated in Figure 5(c). The degree of anisotropy in these plots can be inferred by comparing to the behaviour of the isotropic model shown in Figure 5(d). Note that due to the log-log plot. the equipotential contours in this figure appear "square" instead of circular.

3.2.2. Longitudinal mode of stimulation Next, we examine the effect of model type on the spatial profile of longitudinal membrane potential. To provide a more quantitative view of the behaviour, the longitudinal membrane potential along the fibre (z direction) is presented in Figure 6 for these four models at three electrode-neurite separations, $r = 5\mu$m, $r = 50\mu$m and $r = 100\mu$m (under voltage boundary conditions). These values correspond to the near-field, mid-field and far-field, respectively (for a pulse duration of 100μs; see next subsection on temporal aspects). This figure illustrates that the near-field and far-field models converge to the composite model for small and large electrode-neurite separations, respectively. In mid-field and far-field ranges, the isotropic model not only fails to predict the maximum depolarisation, but also fails to estimate the polarisation extent generated by the extracellular electrical stimulation.

In Figure 7, the maximum depolarisation along a fibre generated by the composite, near-field and far-field models are presented as a function of the electrode-neurite separation for both voltage and current density boundary conditions separately. This figure illustrates that for small values of the electrode-neurite separation (for this case $r < 5\mu$m) the result of the near-field model converges to the composite model (for both voltage and current density boundary conditions). On the other hand, for large values of the electrode-neurite separation (for this case $r > 100\mu$m), the far-field model converges to the membrane potential predicted by the composite model. Therefore, the composite model is interpolating between the near-field and the far-field models for both voltage and current density boundary conditions as shown in Figures 7(a) and 7(b).

3.2.3. Transverse mode of stimulation The transverse component of the membrane potential along the neurite is shown in Figure 8. Again, three electrode-neurite separations, $r = 5\mu$m, $r = 50\mu$m and $r = 100\mu$m, are used, corresponding to near-field, mid-field and far-field (for a pulse width of 100 μs), respectively. This figure shows the differences between the spatial profiles generated by each model along the fibre. Again, there is a good match between the composite model and its near-field and far-field limits, for the corresponding values of r.

The maximum transverse depolarisation along a fibre (i.e., at $z = 0$) as a function of the electrode-neurite separation for the composite model and its extreme limits are shown in Figure 9. It is worth mentioning that for the transverse mode of stimulation,

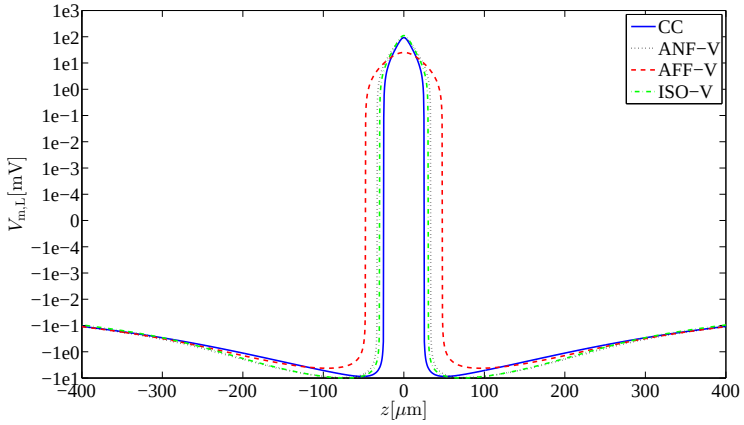

(a)

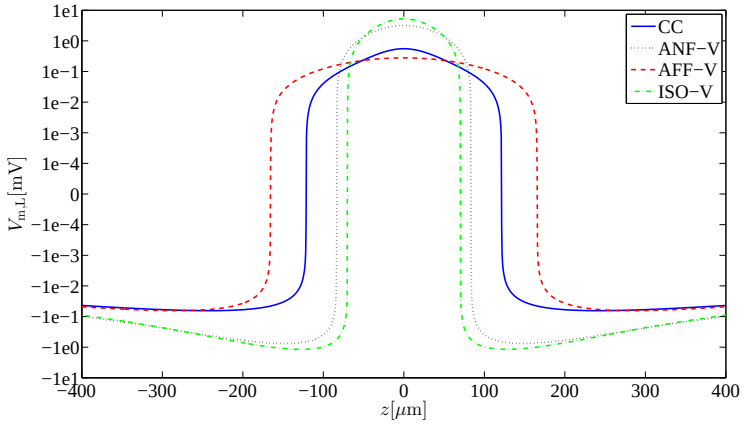

(b)

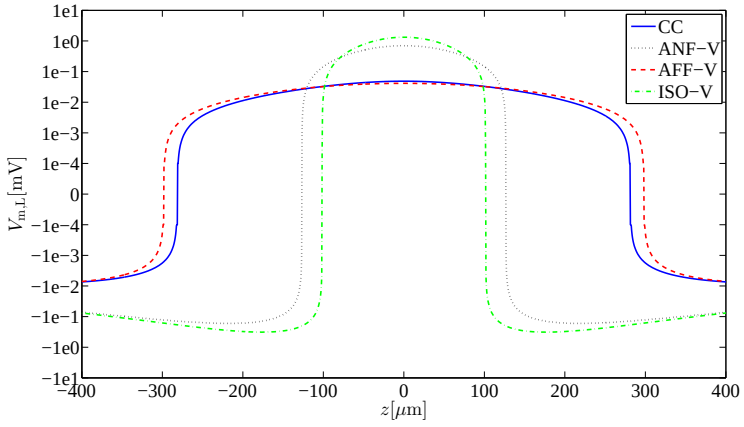

(c)

Figure 6. The longitudinal component of the membrane potential along the fibre for the four models described in the paper under voltage boundary conditions. The electrode-neurite separations are (a) $r = 5\mu$m, (b) $r = 50\mu$m, and (c) $r = 100\mu$m. The membrane potential is mapped linearly for $|V_{\mathrm{m,L}}| < 10^{-4}$mV.

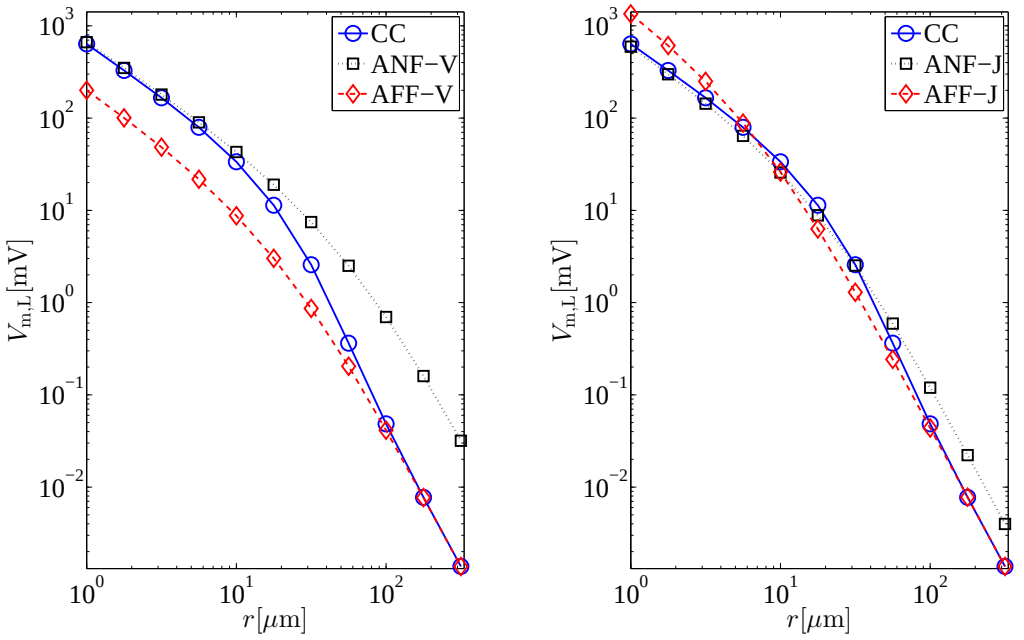

Figure 7. Maximum depolarisation generated by the longitudinal mode of stimulation for the composite model and its two extreme limits, the near-field and far-field models, as a function of electrode-neurite separation, (a) voltage boundary conditions and (b) current density boundary conditions.

the composite, near-field and far-field models are self-consistent and, therefore, one plot is sufficient to show the maximum depolarisation as a function of electrode-neurite separation. Similar to the longitudinal mode, for small and large values of the electrode-neurite separation, $r < 5\mu$m and $r > 100\mu$m, the near-field and far-field models are sufficiently accurate to estimate the transverse component of the membrane potential. Therefore, the composite model is interpolating between the near-field and the far-field models.

3.2.4. Discussion of the results The results show that the membrane potential predicted by the composite model is generally different in magnitude and spatial profile compared to standard models. However, they also show that the near-field and far-field models are simple, yet accurate, approximations to the more complicated composite model for short and long electrode-neurite separations, respectively. Hence, the composite model interpolates between the two asymptotic limits.

Generally, the near-field model predicts greater values for membrane potential than the far-field model. This is because the longitudinal conductivity is less for the near-field model than for its far-field counterpart ($\sigma_{e,L}^{ANF} = 2d/b\rho_e < 1/\rho_i = \sigma_{e,L}^{AFF}$). In terms of the composite model, this reflects that the effective longitudinal conductivity is comparatively low near the electrode, as the current is forced through the confined

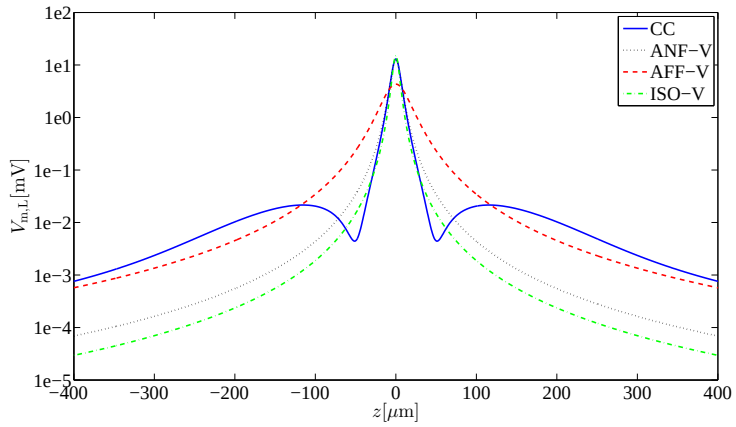

(a)

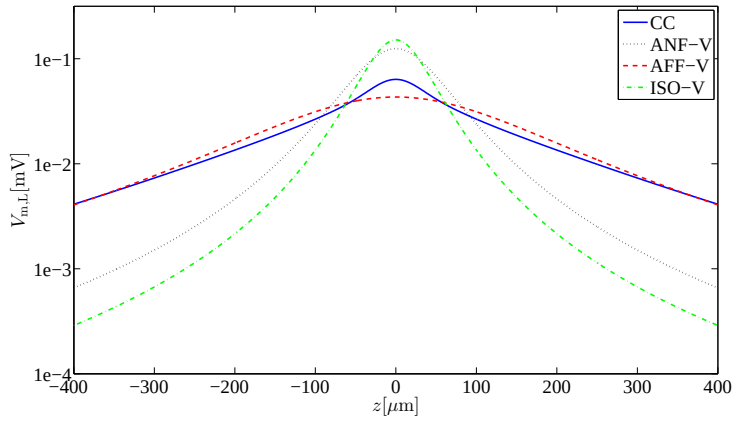

(b)

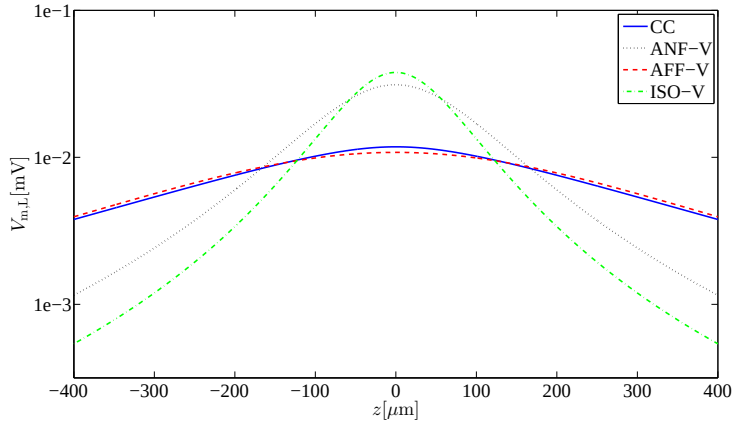

(c)

Figure 8. The transverse component of the membrane potential along the fibre for the four models described in the paper under voltage boundary conditions. The electrode-neurite separations are (a) $r = 5\mu$m, (b) $r = 50\mu$m, and (c) $r = 100\mu$m.

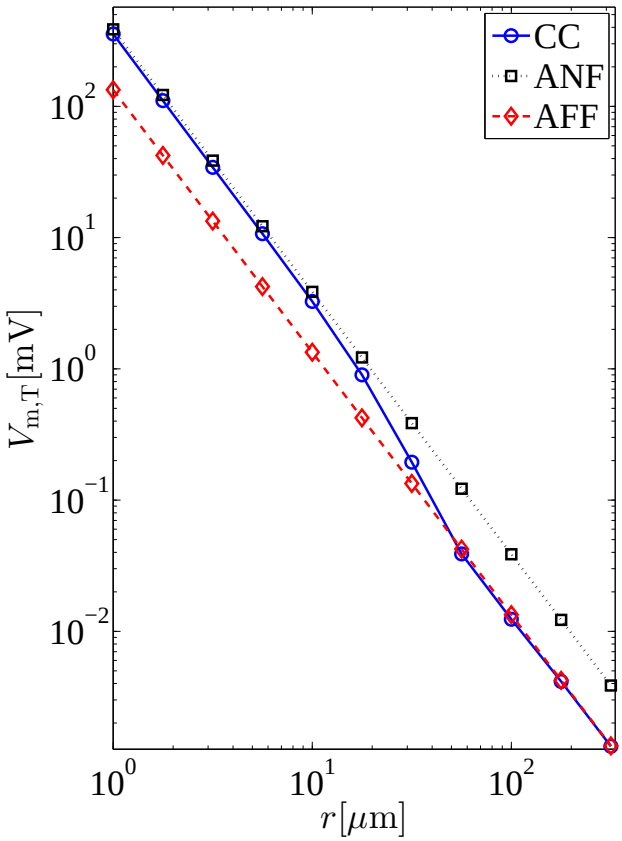

Figure 9. Maximum depolarisation generated by the transverse mode of stimulation for the composite model and its two extreme limits, the near and far-field models, as a function of electrode-neurite separation, r.

extracellular space, but is comparatively large far from the electrode, by which point much of the current has entered the low resistance intracellular pathway along the neurite.

The near-field model is generally much closer to isotropic behaviour than the far-field model. This is reflected in the values of the anisotropy ratio $\chi = \sqrt{2}$ for the near field model and $\chi = \sqrt{b\rho_\mathrm{e}/d\rho_\mathrm{i}} \gg 1$ for the far-field model. Thus, the distribution of V_e and $\mathbf{J}_\mathrm{e}$ is much closer to isotropic in the near-field than the far-field for the composite model. This is expected to have implications for the volume of tissue activated by stimulation, and also for stimulation strategies that rely on the spatial interaction of neighbouring channels to improve spatial selectivity, such "current steering" approaches.

A limitation of the model is that the approximations involved in its derivation limit its validity to values of electrode-neurite separation significantly greater than the radius of an individual neurite ($= 0.5\mu$m here). Consequently predictions for distances closer than 5μm to the electrode should be treated with caution.

An examination of the conditions under which the near-field or far-field limits apply is left to the next subsection, as this depends not only on electrode-neurite separation,

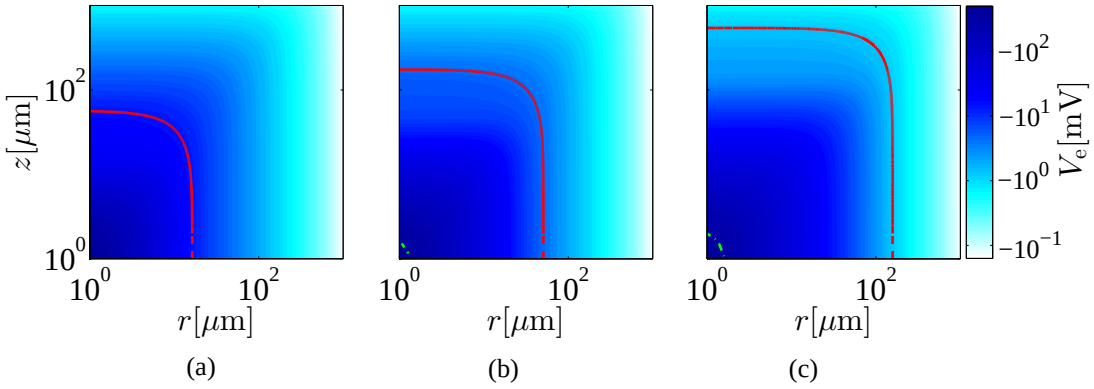

Figure 10. The extracellular potential for the composite model as a function of electrode-neurite separation, r, and distance along the neurite, z, (see Figure 1 for description of r and z) for three different pulse durations (a) $\tau_p = 10\mu$s, (b) $\tau_p = 100\mu$s and (c) $\tau_p = 1$ms. The dash-dotted green lines and dashed red lines show the equipotential lines for the near-field and far-field models, respectively, with 5% error compared to the composite model.

but also on pulse width.

3.3. The short-pulse limit of the composite model is the same as the far-field limit

The longitudinal admittivity of the composite model depends on both temporal and spatial frequency (see Equation (4b)). Consequently, temporal aspects of the stimulus, such as pulse width, can affect the spatial properties of potentials. To examine the effect of pulse width on the spatial distribution of potentials, Figure 10 shows the extracellular potential for the composite model as a function of electrode-neurite separation, r, and distance along the neurite, z, for three different pulse durations: $\tau_p = 10\mu$s, 100μs and 1ms. Also shown on the plot are contours for far-field and near-field limits (as appropriate). The dash-dotted green lines and dashed red lines show the equipotential lines of for the near-field and far-field models, respectively, with 5% error compared to the composite model. Note that for the shortest pulse duration of 10μs, the far-field model provides a good approximation for smaller electrode-neurite separations. The 5% error line for the near-field model for $\tau_p = 10\mu$s is about 1μm in both r and z directions and that is why it is not observed in Figure 10(a). At longer pulse durations, the extracellular potential of the composite model interpolates between the near-field and far-field models as explained in the previous subsection.

Figure 11 shows the longitudinal membrane potential of the composite model as a function of pulse width at an electrode-neurite separation of $r = 50\mu$m. The figure shows that for such a neurite-electrode configuration, the membrane potential can be made to interpolate between the near-field and far-field limits as τ_p is decreased from 1ms to 1μs.

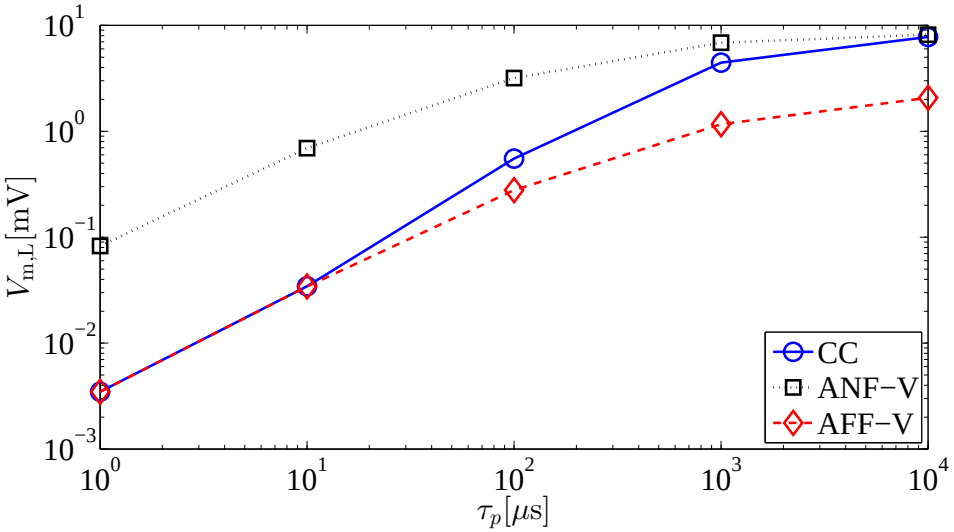

Figure 11. The maximum longitudinal membrane potential for the composite, near-field and far-field models at the end of the cathodic phase. The electrode-neurite separation is $r = 50\mu$m. For the near-field and far-field models, equations for voltage boundary conditions are used.

3.3.1. Discussion of the results The transition in space from near- to far-field must be considered with respect to pulse width. The transition is governed by the separation of the neurite from the electrode, r, relative to the magnitudes of effective electrotonic length constants, which are dependent on temporal frequency:

$$|\lambda_{\mathrm{V}}(\omega)| = \frac{\lambda_{0_{\mathrm{V}}}}{\sqrt{|1 + j\omega\tau_{\mathrm{L}}|}}, \tag{20}$$

$$|\lambda_{\mathrm{J}}(\omega)| = \frac{\lambda_{0_{\mathrm{J}}}}{\sqrt{|1 + j\omega\tau_{\mathrm{L}}|}}. \tag{21}$$

As $|\lambda_{\mathrm{V}}(\omega)| > |\lambda_{\mathrm{J}}(\omega)|$ always, the far-field transition occurs when $r \gg |\lambda_{\mathrm{V}}(\omega)|$ and the near-field transition occurs when $r \ll |\lambda_{\mathrm{J}}(\omega)|$. As pulse widths become shorter, and so the dominant temporal frequencies in spectrum of the pulse get higher, the magnitudes of $\lambda_{\mathrm{V}}(\omega)$ and $\lambda_{\mathrm{J}}(\omega)$ both decrease. Consequently, the transition points for near-field and far-field also decrease (i.e. move nearer to the electrode).

The implication of this for neural stimulation is that pulse duration can affect spatial characteristics of excitation, such as the degree of anisotropy (see discussion in the previous subsection). Conversely, properties of stimulation that are normally considered to be temporal, such as strength-duration curves, can have a dependence of electrode-neurite separation.

3.4. Comparison of the longitudinal and transverse components

Figure 12 shows the transverse-to-longitudinal ratio of the maximum depolarisation along a fibre as a function of the electrode-neurite separation for the standard stimulus at the end of the cathodic phase. Broadly, this figure shows that the longitudinal mode is

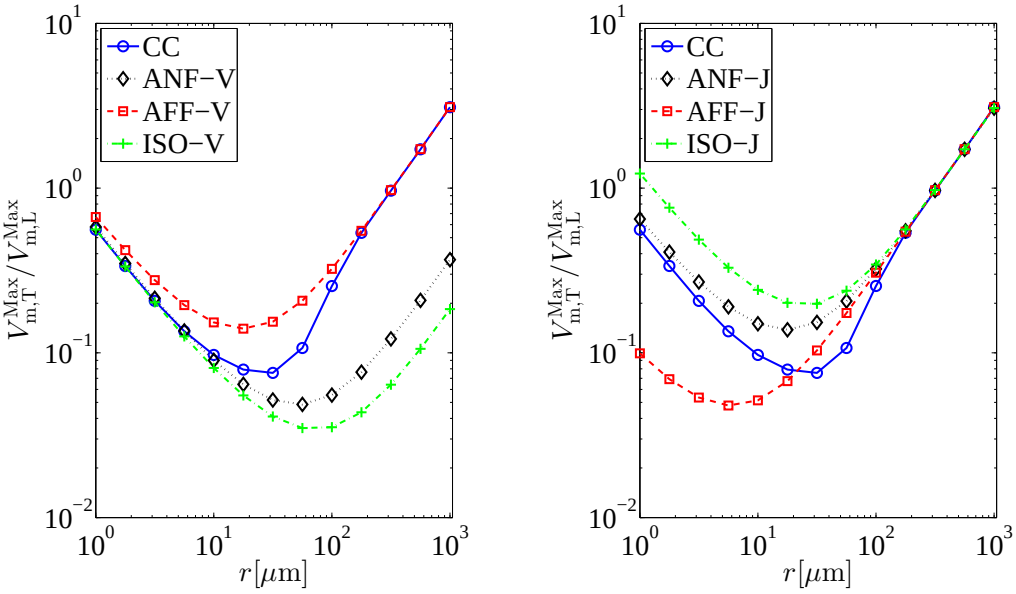

Figure 12. The ratio of the maximum transverse depolarisation to the maximum longitudinal depolarisation for the four models described in this paper. Results for (a) voltage boundary conditions and (b) current density boundary conditions.

comparatively the largest for electrode-neurite separations less than a couple of hundred micrometers (for a pulse width of 100μs). The dominance of the longitudinal model is greatest for separations in ranges of tens of micrometers, corresponding to the mid-range. The transverse mode is comparatively larger in the distant far-field, correspond to separations approaching or exceeding a millimeter.

Interestingly, the ratio for all four models converges to a similar value in the near-field for voltage boundary conditions but not in the far-field. The opposite is true for current density boundary conditions: the ratio converges in the very far-field limit but not in the near field.

Figure 13 shows the relative magnitude of the transverse to the longitudinal components of the membrane potential for different pulse durations, τ_p, and different electrode-neurite separations,r. The composite model is used to compare the magnitudes of these two components. The black line marks the unity ratio. For any values of r and τ_p located above the unity line the transverse mode is the dominant mode of stimulation. This figure illustrates that as the pulse duration decreases, or alternatively, as the electrode-neurite separation increases the transverse mode of stimulation plays a more significant role in stimulating the neurite. The red dash-dotted line indicates the ratio of 10 and the blue dashed line indicates the ratio of 0.1 (the latter meaning that the longitudinal mode is dominating the transverse mode by a factor of 10).

3.4.1. Discussion of the results The composite model suggests that the transverse mode is the dominant mode of stimulation in the far-field limit. On the other hand, in the mid- and near-field range, the longitudinal component is the dominant mode of

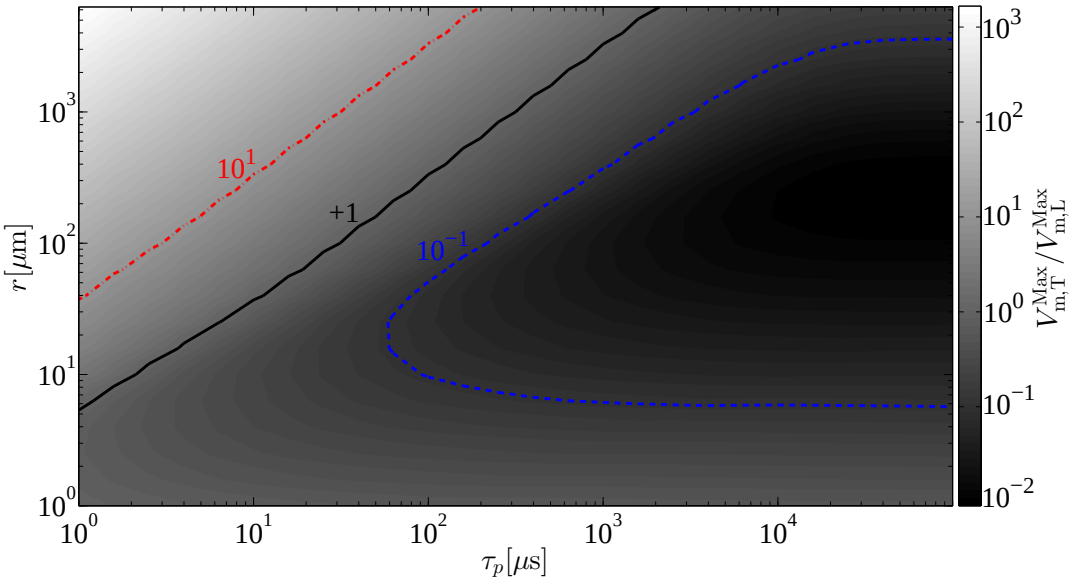

Figure 13. Relative magnitude of the transverse component to the longitudinal component for different pulse durations, τ_p, and different electrode-neurite separations,r, using the composite model. The red, black and blue lines indicate ratios of 10, 1 and 0.1 for the maximum transverse to the maximum longitudinal membrane potential component, respectively.

stimulation. This is broadly consistent with previous theoretical work examining this issue [15, 33]. This result is not consistent across all models presented here as a function of boundary condition type. Thus, a clear prediction on this issue is only possible with the composite model.

Some caution is required in interpreting this result, because the transduction of the passive (subthreshold) membrane potential into an action potential has not been modelled here. The thresholds for spike initiation may differ for the longitudinal and traverse modes of stimulation, thus further work is required to clarify this result (see [34]).

3.5. The time behaviour of the fibre response can be significantly affected by the temporal filtering of the tissue in the composite model

To inspect the time behaviour of each model during and after the stimulation period, we plotted the membrane potential for each model under voltage and current density boundary conditions for $r = 50\mu$m. In order to provide more insight to the time behaviour of the membrane potential, we applied cathodic first biphasic stimuli with three different pulse durations, $\tau_p = 10\mu$s, $\tau_p = 100\mu$s and $\tau_p = 1$ms.

3.5.1. Longitudinal mode of stimulation The time behaviour for the longitudinal component of stimulation is shown in Figure 14. We have normalised the membrane

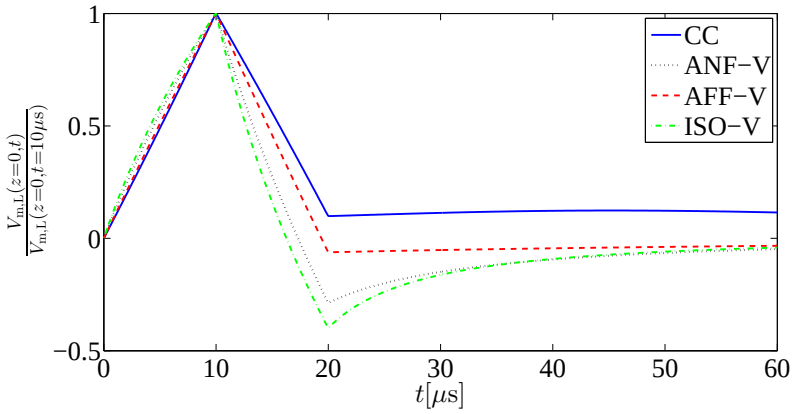

(a)

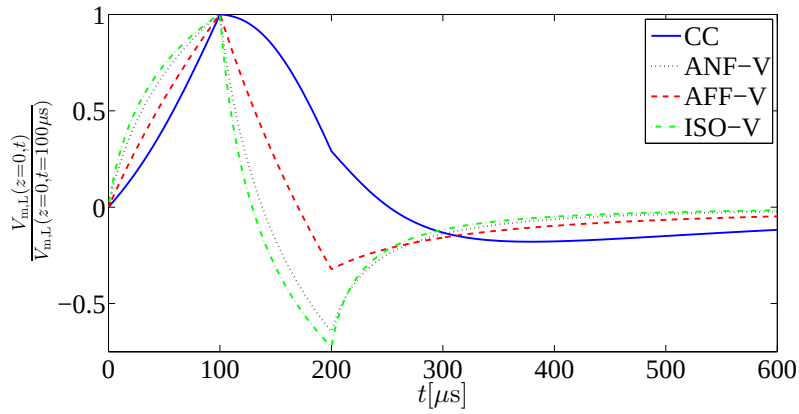

(b)

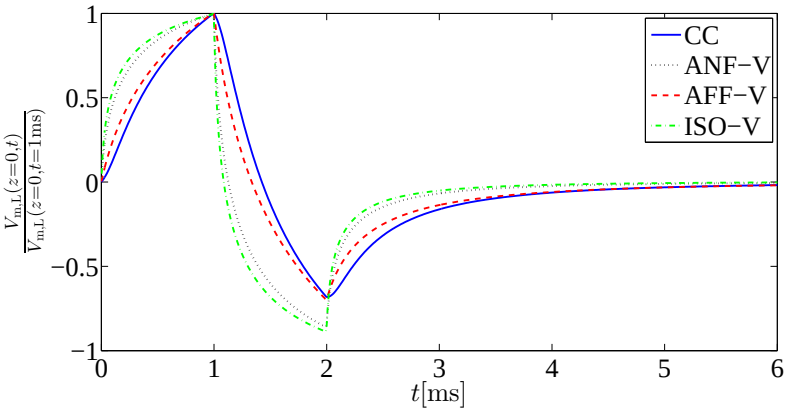

(c)

Figure 14. The time behaviour of the normalised longitudinal mode of stimulation under voltage boundary conditions for the four models described in the paper. The applied stimulus is a first cathodic biphasic pulse where the pulse duration is (a) $\tau_p = 10\mu$s, (b) $\tau_p = 100\mu$s and (c) $\tau_p = 1$ms.

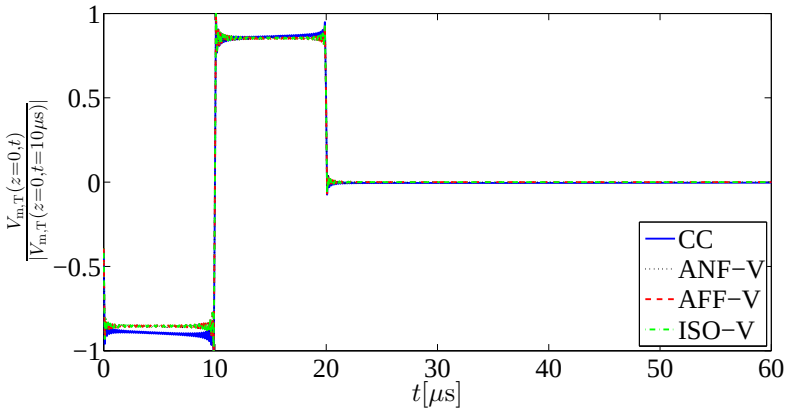

(a)

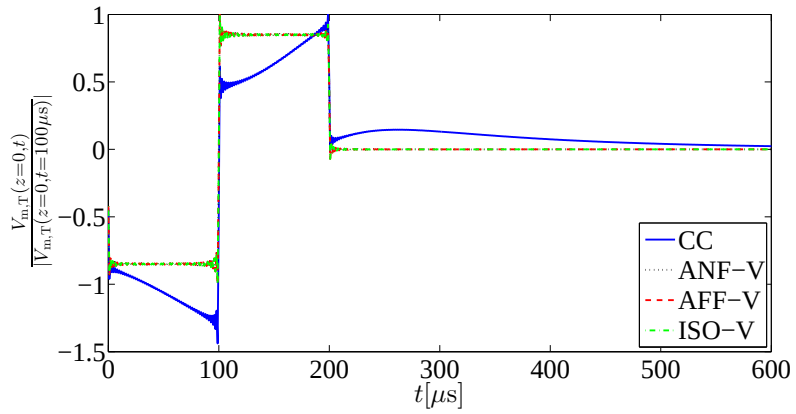

(b)

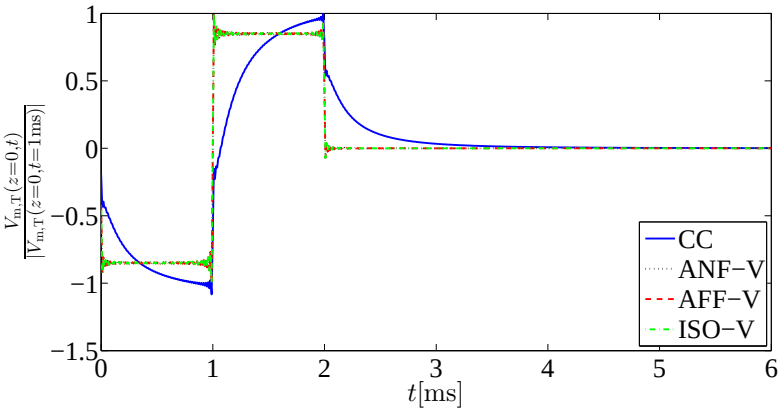

(c)

Figure 15. The time behaviour of the normalised transverse mode of stimulation under voltage boundary conditions for the four models described in the paper. The applied stimulus is a first cathodic biphasic pulse where the pulse duration is (a) $\tau_p = 10\mu$s, (b) $\tau_p = 100\mu$s and (c) $\tau_p = 1$ms.

potential for each model,so that the waveforms of all models can be compared more easily.

3.5.2. Transverse mode of stimulation Figure 15 shows the time behaviour of the transverse component of stimulation for three different pulse duration, (a) $\tau_p = 10\mu$s, (b) $\tau_p = 100\mu$s and (c) $\tau_p = 1$ms. Given that for standard models the tissue is purely resistive, the transverse component follows the stimulus in time as shown in Figure 15.§ However, the capacitive behaviour of the tissue is reflected in the transverse mode of stimulation for the composite model. For short pulses, the electric impedance of the capacitor is small and, therefore, the transverse mode response is more resistive and follows the stimulus in time as illustrated in Figure 15(a). On the other hand, for long duration stimulus, the electric impedance of the capacitor is large and, therefore, the transverse mode response in time is over-damped as demonstrated in Figure 15(c).

3.5.3. Discussion of the results An important feature present in the response of the composite model and partially in its far-field limit is its behaviour during the anodic phase of stimulation. In contrast to the isotropic volume conductor model that the longitudinal membrane potential follows the stimulus waveform in time, for short pulse durations there is no hyperpolarising effect in the second phase of stimulation when the composite model is applied. For intermediate pulses, the hyperpolarising effect is negligible. Moreover for all pulse durations the composite model response experiences a lag in the membrane potential response due to the capacitive features that are considered for neural tissue in this approach compared to other models for tissue that are purely resistive.

4. Discussion

We presented simulation results for a point source stimulus in neural tissue with typical parameters. We compared the result of the composite model to standard volume conductor models and showed how the spatio-temporal pattern of stimulation differs for each model. Modeling extracellular electrical stimulation and estimating the resultant neural activity have been studied by many researchers in the field [6–8, 14, 15, 33, 35–44].

Isotropic monodomain, anisotropic monodomain, and anisotropic bidomain models to estimate the extracellular potential under a point source stimulation for a fibre bundle was studied by Altman and Plonsey [8, 14, 45, 46] for a fibre-bundle. Their bidomain model results demonstrate a considerable difference with the isotropic volume conductor model. The passive version of their model is formally equivalent to the composite volume conductor model used here for the case of tissue composed of identical parallel fibres (see companion paper [16]). The results present in this paper confirm their earlier conclusions that the confined extracellular space has significant impact on the spatial

§ The ringing effect in the transverse mode is due to numerical errors associated with discrete inverse Fourier transform calculation (Gibbs phenomenon).

profile of neural activation in a fibre-bundle compared to standard models. They also extend their model considering non-steady state behaviour (i.e. stimulation pulses of finite duration), by providing a description of the transverse mode of stimulation and by clearly describing the near- and far-field limits of these models (corresponding to the "mono-domain" and "modified mono-domain" models in [46]). More generally, the modeling framework described in [16] generalises the bidomain model in [14] to multidomain models that apply to situations in which the tissue comprises arbitrary mixtures of neurites with different orientations, sizes and electrical properties. It also provides an equivalent volume conductor description for these more complex tissue types by introducing a single aggregate admittivity kernel relating the extracellular current density and potential.

It was shown in [40, 47] that anisotropy of fibre bundles should be considered in finding the current spread in tissue as a result of electrical stimulation. Therefore, it was suggested that both intracellular and extracellular volumes should be modeled by conductivity tensors. They have used experimental data to model the conductivity of the tissue. In this paper, we calculated the elements of the admittivity tensor from the microstructural properties of the tissue. Therefore, our model incorporates the anisotropy of neural tissue.

In [43], the permittivity of the tissue is taken into account for estimating the extracellular potential. In particular, a dependence of the permittivity on temporal frequency is introduced. Simulation results show that there is a clear difference between the extracellular potential calculated for purely resistive tissue and tissue with capacitive features (see Figure 2 in [43]). They solved an inhomogeneous Helmholtz equation to compare the extracellular potential to the quasi-static solution (isotropic volume conductor model). Their simulation results show up to 13% difference between the two solutions. This agrees with the composite model, which has non-instantaneous properties and takes into account the capacitive properties of the tissue. In addition, the admittivity tensor for the composite model introduced here has a dependency of spatial frequency that is not present in [43].

The 'whole finite element approach' is introduced in [44], which considers the presence of the neurite in estimating the membrane potential. They compared the whole finite element approach to the two stage or hybrid model and demonstrated that the finite element model provides a more detailed description of the membrane potential. This is in agreement with the composite model results, which show that considering the presence of the neurite alters the response of the neurite compared to a standard volume conductor model.

5. Conclusion

In this paper, we considered how the cellular composition of tissue effects the spatio-temporal response of neural tissue under extracellular electrical stimulation. This was done by comparing the response of a non-standard volume conductor model

derived in [16] to three standard volume conductor models for the case of point source stimulation of a bundle of tightly packed parallel fibres. The non-standard model, termed the cellular composite model captures the effects of the cellular composition to tissue in detail, whereas the standard models provide approximations in either near- or far-field, or do not attempt to capture these effects except in a crude fashion (the isotropic model). The main conclusions are as follows:

- Only the composite model provides a self-consistent prediction for the subthreshold membrane potential over the full range of electrode-neurite separations. That is, only the composite model predicts the same membrane potential, regardless of whether the extracellular voltage or the extracellular current density from Stage 1 of the model is used as a boundary condition in Stage 2. The near- and far-field models are self-consistent in the near- and far-fields, respectively. Other than this the standard models give different predictions that can differ from the cellular composite model and from each other by several hundred percent. Consequently the cellular composite model should used whenever a large range of electrode-neurite separations are of interest. When the only separations of interest are either close to or far from the electrode, then an anisotropic volume conductor model is a good approximation.
- The cellular composite model interpolates between the near- and far-field approximations. The transition to the near-field occurs when the electrode-neurite separation $r \ll |\lambda_J(\omega)|$ (= frequency-dependent effective electronic length constant for current density boundary conditions). The transition to the far-field occurs when $r \gg |\lambda_V(\omega)|$ (= equivalent for voltage boundary conditions). Thus the transition points depend on the pulse duration through its spectral frequency content, and can vary from 10s of microns for high frequencies to many hundreds of microns for low frequencies [48].
- In the near-field the effective conductivity and degree of anisotropy is lower and than in the far-field. This is because the current is forced to pass through the confined extracellular space in the near-field, but can access the low resistance, longitudinally oriented intracellular space in the far-field.
- The longitudinal component of the subthreshold membrane potential is greater than the transverse component in the near- and mid-field, whereas the transverse component is greatest in distant far-field. Further work is required to determine if this result applies to the supra-threshold spiking activity of neurons.
- The temporal filtering properties of the tissue in the composite model can significantly alter the waveforms for the subthreshold membrane potential relative to standard models.

6. Acknowledgements

This research was supported by the Australian Research Council (ARC) through its Special Research Initiative (SRI) in Bionic Vision Science and Technology grant to Bionic Vision Australia (BVA). The Bionics Institute acknowledges the support it receives from the Victorian Government through its Operational Infrastructure Support Program. This research was supported by a Victorian Life Sciences Computation Initiative (VLSCI) grant number VR0138 on its Peak Computing Facility at the University of Melbourne, an initiative of the Victorian Government.

Appendix A. Why standard volume conductor models result in inconsistent membrane potential?

In [17, 18], we derived two sets of equations for the membrane potential under current density and voltage boundary conditions from Maxwell's equations. These equations for the longitudinal and the transverse components are summarised in Table 2 of this paper. Given that the membrane potential must be the same regardless of the type of the boundary conditions used, we showed that the longitudinal and transverse components of the extracellular potential and current density should satisfy the following equations (trans-impedance of the neurite plus thin extracellular sheath)

$$\text{Longitudinal:} \qquad \hat{\tilde{V}}_{\mathrm{e,L}}(k_z,\omega) = -\frac{2\rho_i}{k_z^2 b}\left(\frac{1+k_z^2\lambda_V^2(\omega)}{1+k_z^2\lambda_J^2(\omega)}\right)\hat{\tilde{J}}_{\mathrm{e,L}}(k_z,\omega), \tag{A.1a}$$

$$\text{Transverse:} \qquad \hat{\tilde{V}}_{\mathrm{e,T}}(k_z,\omega) = -R_{e,J}(1)\hat{\tilde{J}}_{\mathrm{e,T}}(k_z,\omega). \tag{A.1b}$$

Therefore, by considering the neurite alone (regardless of the surrounding tissue), if one stipulates V_e on the boundary of the neurite, then J_e is fixed as well and vice versa. An isotropic volume conductor will give a solution that for V_e and J_e will not satisfy the above equations as these equations are different in the longitudinal versus transverse directions. More generally, the volume conductor model will give V_e and J_e satisfying these equations, if and only if, the transimpedance of the volume displacing the neurite in the volume conductor matches the transimpedance of the actual neurite in the longitudinal and transverse directions, as given by Equation (A.1a).

In [16], we derived the composite model that takes into account the presence of the neurite. In this paper, we showed that the Anisotropic Near-Field (ANF) and the Anisotropic Far-Field (AFF) models of neural tissue extracted from the composite model result in consistent membrane potentials when the electrode-neurite separation is small or large, respectively.

Appendix A.1. Analogy example

Consider the electric circuit shown in Figure 1(a) where R_N is a nonlinear resistor where its voltage, V_{R_N}, and current, I_{R_N}, are related through $V_{R_N} = f(I_{R_N})$ in which

Table A1. Duality table for neural tissue and the electric circuit shown in Figure A1.

Neural Tissue	Electric Circuit
The trans-impedance of a neurite (Equation(A.1a))	Nonlinear resistor (R_N)
Conductivity of isotropic tissue	Linear resistor (R_T)
Current point source (I)	Voltage source (V_0)
Voltage boundary condition on the neurite (V_e)	Voltage across the resistor (V_{R_N})
Current density boundary condition on the neurite (J_e)	Current passing through the resistor (I_{R_N})
Membrane potential (V_m) for current density or voltage boundary conditions	Power dissipated by the resistor (P_I or P_V)

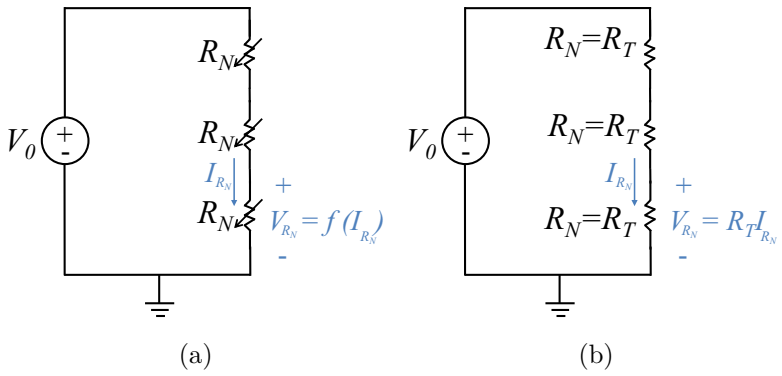

Figure A1. The electric circuit for the analogy example. (a) Circuit with a nonlinear resistor and (b) the simplified circuit to calculate the voltage or current of the nonlinear resistor by replacing R_N with the linear resistor R_T. The duality relation between this circuit and neural tissue is given in Table A1.

$f(\cdot)$ is a nonlinear function. It should be noted that in subthreshold models including two-stage volume conductor model there is no nonlinearity in any stage of the model. Here, we introduce nonlinearity to give a non-trivial electric circuit example. This is the dual of the trans-impedance of the neurite indicated by Equation (A.1a) and does not mean that neural tissue in our model is nonlinear. We mainly want to emphasis that it is complicated. The objective is to calculate the power dissipated by the nonlinear resistor, R_N. The duality relation between this example and neural tissue is given in Table A1.

Similar to neural tissue, for simplicity, one may decide to solve the problem in two

stages. In Stage 1, the nonlinear resistor is replaced by R_T (Tissue resistivity) as shown in Figure 1(b) to calculate the voltage across this resistor or the current passing through it. In Stage 2, the power is calculated for the nonlinear resistor.

In Stage 1, we calculate V_{R_N} to be

$$V_{R_N} = \frac{V_0}{3}, \tag{A.2}$$

where V_0 is the magnitude of the voltage source. In the second stage, the dissipated power for R_N using the calculated voltage is

$$P_V = V_{R_N} I_{R_N} = \frac{V_0}{3} f^{-1}\left(\frac{V_0}{3}\right), \tag{A.3}$$

where $f^{-1}(\cdot)$ is the inverse function of $f(\cdot)$.

Alternatively, we can calculate I_{R_N} in Stage 1,

$$I_{R_N} = \frac{V_0}{3R_T}, \tag{A.4}$$

and use current to find the dissipated power,

$$P_I = V_{R_N} I_{R_N} = f\left(\frac{V_0}{3R_T}\right)\frac{V_0}{3R_T}. \tag{A.5}$$

The calculated V_{R_N} and I_{R_N} in the first stage satisfy Kirchhoff's voltage and current laws and in the second stage we used the same equation to calculate the dissipated power. However, the calculated powers using voltage or current from the first stage are inconsistent, $P_V \neq P_I$. Moreover, both are incorrect values for dissipated power. For the same reason, when a neurite is replaced with an isotropic volume conductor to calculate the extracellular voltage or current density, the resultant membrane potential is inconsistent depending on the type of the boundary conditions used, and both are inaccurate.

Appendix B. Calculating the membrane potential

By substituting the continuity equation into the constitutive equation in the Fourier domain, we obtain

$$\begin{aligned}\check{\boldsymbol{\nabla}} \cdot \hat{\hat{\boldsymbol{\xi}}}_{\mathrm{e}} \check{\boldsymbol{\nabla}} \hat{\hat{V}}_{\mathrm{e}} &= \begin{bmatrix} \dfrac{\partial}{\partial x} \\ \dfrac{\partial}{\partial y} \\ jk_z \end{bmatrix} \cdot \begin{bmatrix} \hat{\hat{\xi}}_{\mathrm{e,T}} & 0 & 0 \\ 0 & \hat{\hat{\xi}}_{\mathrm{e,T}} & 0 \\ 0 & 0 & \hat{\hat{\xi}}_{\mathrm{e,L}}(k_z,\omega) \end{bmatrix} \begin{bmatrix} \dfrac{\partial \hat{\hat{V}}_{\mathrm{e}}(x,y,k_z,\omega)}{\partial x} \\ \dfrac{\partial \hat{\hat{V}}_{\mathrm{e}}(x,y,k_z,\omega)}{\partial y} \\ jk_z \end{bmatrix} \\ &= \hat{\hat{\xi}}_{\mathrm{e,T}} \left(\frac{\partial^2 \hat{\hat{V}}_{\mathrm{e}}(x,y,k_z,\omega)}{\partial^2 x} + \frac{\partial^2 \hat{\hat{V}}_{\mathrm{e}}(x,y,k_z,\omega)}{\partial^2 y} \right) - \hat{\hat{\xi}}_{\mathrm{e,L}}(k_z,\omega) k_z^2 \hat{\hat{V}}_{\mathrm{e}} = 0, \end{aligned} \tag{B.1}$$

which in cylindrical coordinates may be written as

$$\hat{\hat{\xi}}_{\mathrm{e,T}}\left(\frac{1}{r}\frac{\partial}{\partial r}\Big(r\frac{\partial\hat{\hat{V}}_{\mathrm{e}}(r,k_z,\omega)}{\partial r}\Big)\right)-\hat{\hat{\xi}}_{\mathrm{e,L}}(k_z,\omega)\;k_z^2\;\hat{\hat{V}}_{\mathrm{e}}(r,k_z,\omega)=0, \tag{B.2}$$

or, equivalently,

$$\frac{\partial^2\hat{\hat{V}}_{\mathrm{e}}(r,k_z,\omega)}{\partial r^2}+\frac{1}{r}\frac{\partial\hat{\hat{V}}_{\mathrm{e}}(r,k_z,\omega)}{\partial r}-\frac{\hat{\hat{\xi}}_{\mathrm{e,L}}(k_z,\omega)}{\hat{\hat{\xi}}_{\mathrm{e,T}}}\;k_z^2\;\hat{\hat{V}}_{\mathrm{e}}(r,k_z,\omega)=0. \tag{B.3}$$

The above equation is the Modified Bessel's Equation with $n=0$. Therefore, the general solution can be expressed by

$$\hat{\hat{V}}_{\mathrm{e}}(r,k_z,\omega)=A(k_z)\;I_0\Big(\hat{\hat{\chi}}(k_z,\omega)r|k_z|\Big)+B(k_z)\;K_0\Big(\hat{\hat{\chi}}(k_z,\omega)r|k_z|\Big), \tag{B.4}$$

where

$$\hat{\hat{\chi}}(k_z,\omega)\triangleq\sqrt{\frac{\hat{\hat{\xi}}_{\mathrm{e,L}}(k_z,\omega)}{\hat{\hat{\xi}}_{\mathrm{e,T}}}}. \tag{B.5}$$

and I_0 and K_0 are the zeroth order of the modified Bessel's functions of the first and second kind, respectively. The coefficients $A(k_z)$ and $B(k_z)$ are constants to be determined. Given that I_0 is unbounded as $r\to\infty$, therefore $A(k_z)=0$ for all values of k_z. Assuming that the current source is surrounded by an infinite cylinder, we may write

$$\begin{aligned}\hat{I}(\omega)=\oint_S\hat{\mathbf{J}}_{\mathrm{e}}\cdot d\mathbf{s}=\int_0^{2\pi}\int_{z=-\infty}^{z=\infty}\hat{\mathbf{J}}_{\mathrm{e}}(r,z,\omega)\cdot\mathbf{n}\,r\,dz\,d\theta&=\int_0^{2\pi}r\,d\theta\int_{z=-\infty}^{z=\infty}\hat{\mathbf{J}}_{\mathrm{e}}(r,z,\omega)\cdot\mathbf{n}\,dz\\&=2\pi\sqrt{2\pi}\,r\,\hat{\hat{\mathbf{J}}}_{\mathrm{e}}(r,k_z=0,\omega)\cdot\mathbf{n}.\end{aligned} \tag{B.6}$$

Taking into account that

$$\begin{aligned}\hat{\hat{\mathbf{J}}}_{\mathrm{e}}(r,k_z,\omega)\cdot\mathbf{n}\Big|_r=-\hat{\hat{\xi}}_{\mathrm{e,T}}\nabla\hat{\hat{V}}_{\mathrm{e}}(r,k_z,\omega)\Big|_r&=-\hat{\hat{\xi}}_{\mathrm{e,T}}\frac{\partial\hat{\hat{V}}_{\mathrm{e}}(r,k_z,\omega)}{\partial r}\\&=-B(k_z)\,\hat{\hat{\xi}}_{\mathrm{e,T}}\,\hat{\hat{\chi}}(k_z,\omega)|k_z|\;K_0'\left(\hat{\hat{\chi}}(k_z,\omega)r|k_z|\right),\end{aligned} \tag{B.7}$$

and, therefore,

$$r\,\hat{\hat{\mathbf{J}}}_{\mathrm{e}}(r,k_z=0,\omega)\cdot\mathbf{n}=\lim_{k_z\to0}-B(k_z)\,\hat{\hat{\xi}}_{\mathrm{e,T}}\,\hat{\hat{\chi}}(k_z,\omega)r|k_z|\;K_0'\left(\hat{\hat{\chi}}(k_z,\omega)r|k_z|\right)=B(0)\hat{\hat{\xi}}_{\mathrm{e,T}}. \tag{B.8}$$

Thus, $B(0)$ is calculated to be

$$B(0)=\frac{\hat{I}(\omega)}{4\pi\hat{\hat{\xi}}_{\mathrm{e,T}}}\sqrt{\frac{2}{\pi}}. \tag{B.9}$$

Therefore, $\hat{\hat{V}}_{\mathrm{e}}(r,k_z,\omega)$ is given by Equation (6).

Appendix C. Near-field and far-field approximations

Given that $\mathbf{J}_\mathrm{e}$ and $\boldsymbol{\nabla} V_\mathrm{e}$ are both odd functions in terms of z and both are absolutely integrable, their Fourier transform can be expressed in Laplace domain. For a general case when $h(z) = g(z) * f(z)$, in the near-field approximation, the objective is to find a g^{NF} for small values of z such that

$$g^{\mathrm{NF}} = \frac{\lim_{z\to 0} h(z)}{\lim_{z\to 0} f(z)}. \tag{C.1}$$

Using the initial value theorem in Laplace domain [49] results in

$$g^{\mathrm{NF}} = \frac{\lim_{z\to 0} h(z)}{\lim_{z\to 0} f(z)} = \frac{\lim_{s\to\infty} sH(s)}{\lim_{s\to\infty} sF(s)} = \frac{\lim_{s\to\infty} sG(s)F(s)}{\lim_{s\to\infty} sF(s)}, \tag{C.2}$$

where $H(s)$, $G(s)$ and $F(s)$ are Laplace transforms of $h(t)$, $g(t)$ and $f(t)$, respectively. Given that $\lim\limits_{x\to a}\Big(f_1(x)\cdot f_2(x)\Big) = \lim\limits_{x\to a} f_1(x)\cdot \lim\limits_{x\to a} f_1(x)$, therefore,

$$g^{\mathrm{NF}} = \lim_{s\to\infty} G(s), \tag{C.3}$$

where in the Fourier domain translates to

$$g^{\mathrm{NF}} = \lim_{k_z\to\infty} G(jk_z). \tag{C.4}$$

The same argument is valid for the far-field limit if the final value theorem [49] is used. It should be noted that the $1/2\pi$ factor in Equation (1a) does not affect the above argument.

References

[1] J. Rizzo, J. Tombran-Tink, and C.J. Barnstable. *Visual Prosthesis and Ophthalmic Devices: New Hope in Sight*. Ophthalmology Research. Humana, 2007.

[2] J.K. Niparko. *Cochlear Implants: Principles & Practices*. Williams & Wilkins, 2nd edition, 2009.

[3] J.P. Reilly and A.M. Diamant. *Electrostimulation: Theory, Applications, and Computational Models*. Artech House, 2011.

[4] N. Trayanova, C.S. Henriquez, and R. Plonsey. Extracellular potentials and currents of a single active fiber in a restricted volume conductor. *Annals of Biomedical Engineering*, 18(3):219 – 238, 1990.

[5] F. Rattay. *Electrical Nerve Stimulation : Theory, Experiments and Applications*. Springer-Verlag, 1990.

[6] J.T. Rubinstein and F.A. Spelman. Analytical theory for extracellular electrical stimulation of nerve: I. Passive unmyelinated axon. *Biophysical Journal*, 54(6):975–981, 1988.

[7] J.T. Rubinstein. Analytical theory for extracellular electrical stimulation of nerve: II. Passive myelinated axon. *Biophysical Journal*, 60(3):538–555, 1991.

[8] K.W. Altman and R. Plonsey. Development of a model for point source electrical fibre bundle stimulation. *Medical & Biological Engineering & Computing*, 26(5):466–475, 1988.

[9] Sébastien Joucla and Blaise Yvert. Modeling extracellular electrical neural stimulation: From basic understanding to MEA-based applications. *Journal of Physiology-Paris*, 106:146 – 158, 2012.

[10] J.B. Ranck, Jr. Specific impedance of rabbit cerebral cortex. *Experimental Neurology*, 7(2):144–152, 1963.

[11] J. Lattika, T. Kuurne, and H. Eskola. Conductivity of living intracranial tissues. *Physics in Medicine and Biology*, 46(6):1611–1616, 2001.

[12] C. Gabriel, A. Peyman, and E.H. Grant. Electrical conductivity of tissue at frequencies below 1 MHz. *Physics in Medicine and Biology*, 54(16):4863–4878, 2009.

[13] H. Meffin, B. Tahayori, D.B. Grayden, and A.N. Burkitt. Internal inconsistencies in models of electrical stimulation in neural tissue. In *Engineering in Medicine and Biology Society (EMBC), 2013 Annual International Conference of the IEEE*, pages 5946–5949, 2013.

[14] K.W. Altman and R. Plonsey. Point source nerve bundle stimulation: effects of fiber diameter and depth on simulated excitation. *Biomedical Engineering, IEEE Transactions on*, 37(7):688–698, July 1990.

[15] V. Schnabel and J.J. Struijk. Evaluation of the cable model for electrical stimulation of unmyelinated nerve fibers. *IEEE Transactions on Bio-Medical Engineering*, 48(9):1027 – 1033, 2001.

[16] H. Meffin, B. Tahayori, E.N. Sergeev, Iven M.Y. Mareels, D.B. Grayden, and A.N. Burkitt. Modeling extracellular electrical stimulation: III. Derivation and interpretation of neural tissue equations. *Journal of Neural Engineering*, 2014.

[17] H. Meffin, B. Tahayori, D.B. Grayden, and A.N. Burkitt. Modeling extracellular electrical stimulation: I. Derivation and interpretation of neurite equations. *Journal of Neural Engineering*, 9:065005, 2012.

[18] B. Tahayori, H. Meffin, S. Dokos, D.B. Grayden, and A.N. Burkitt. Modeling extracellular electrical stimulation: II. Computational validation and numerical results. *Journal of Neural Engineering*, 9:065006, 2012.

[19] A. Faisal, J. White, and S. Laughlin. Ion-channel noise places limits on the miniaturization of the brain's wiring. *Current Biology*, 15(12):1143–1149, 2005.

[20] J.A. Perge, K. Koch, R. Miller, P. Sterling, and V. Balasubramanian. How the optic nerve allocates space, energy capacity, and information. *The Journal of Neuroscience*, 29(24):7917–7928, 2009.

[21] J.A. Perge, J.E. Niven, E. Mugnaini, V. Balasubramanian, and P. Sterling. Why do axons differ in caliber? *The Journal of Neuroscience*, 32(2):626–638, 2012.

[22] Y. Assaf, T. Blumenfeld-Katzir, Y. Yovel, and P.J. Basser. AxCaliber: a method for measuring axon diameter distribution from diffusion MRI. *Magnetic Resonance in Medicine*, 59(6):1347–1354, 2008.

[23] E. Sykova and C. Nicholson. Diffusion in brain extracellular space. *Physiological Reviews*, 88(4):1277 – 1340, 2008.

[24] G. Stuart and N. Spruston. Determinants of voltage attenuation in neocortical pyramidal neuron dendrites. *The Journal of Neuroscience*, 18(10):3501–3510, 1998.

[25] D.P. Shelton. Membrane resistivity estimated for the Purkinje neuron by means of a passive computer model. *Neuroscience*, 14(1):111–131, 1985.

[26] D. Thurbon, H.R. Lüscher, T. Hofstetter, and S.J. Redman. Passive electrical properties of ventral horn neurons in rat spinal cord slices. *Journal of Neurophysiology*, 79:2485–2502, 1998.

[27] R. Gleixner and P. Fromherz. The extracellular electrical resistivity in cell adhesion. *Biophysical Journal*, 90(7):2600–2611, 2006.

[28] R.A. Chitwood, A. Hubbard, and D.B. Jaffe. Passive electrotonic properties of rat hippocampal CA3 interneurones. *The Journal of Physiology*, 515(3):743–756, 1999.

[29] W.R. Taylor, S. Mittman, and D.R. Copenhagen. Passive electrical cable properties and synaptic excitation of tiger salamander retinal ganglion cells. *Visual Neuroscience*, 13(5):979–90, 1996.

[30] J.N. Barrett and W.E. Crill. Specific membrane resistivity of dye-injected cat motoneurons. *Brain Research*, 28(3):556–561, 1971.

[31] T. Omori, T. Aonishi, H. Miyakawa, M. Inoue, and M. Okada. Estimated distribution of specific membrane resistance in hippocampal ca1 pyramidal neuron. *Brain Research*, 1125(1):199 – 208,

2006.

[32] L.J. Gentet, G.J. Stuart, and J.D. Clements. Direct measurement of specific membrane capacitance in neurons. *Biophysical Journal*, 79(1):314–320, 2000.

[33] L.M. Livshitz, P.D. Einziger, and J. Mizrahi. Rigorous green's function formulation for transmembrane potential induced along a 3-d infinite cylindrical cell. *IEEE Transactions on Biomedical Engineering*, 49(12):1491, 2002.

[34] E.N. Sergeev, H. Meffin, B. Tahayori, D.B. Grayden, and A.N. Burkitt. Effect of soma polarization on electrical stimulation thresholds of retinal ganglion cells. In *6th International IEEE/EMBS Conference on Neural Engineering (NER)*, pages 1135–1138, Nov 2013.

[35] D.R. McNeal. Analysis of a model for excitation of myelinated nerve. *IEEE Transactions on Biomedical Engineering*, 23(4):329 – 337, 1976.

[36] F. Rattay. Analysis of models for external stimulation of axons. *IEEE Transactions on Bio-Medical Engineering*, 33(10):974 – 977, 1986.

[37] F. Rattay. Simulation of artificial neural reactions produced with electric fields. *Simulation Practice and Theory*, 1:137 – 152, 1993.

[38] F. Rattay. The basic mechanism for the electrical stimulation of the nervous system. *Neuroscience*, 89(2):335 – 346, 1999.

[39] E.N. Warman, W.M. Grill, and D. Durand. Modeling the effects of electric fields on nerve fibers: Determination of excitation thresholds. *Biomedical Engineering, IEEE Transactions on*, 39(12):1244–1254, Dec 1992.

[40] B.J. Roth. How the anisotropy of the intracellular and extracellular conductivities influences stimulation of cardiac muscle. *Journal of Mathematical Biology*, 30(6):633–646, 1992.

[41] P.J. Basser and B.J. Roth. New currents in electrical stimulation of excitable tissues. *Annual Review of Biomedical Engineering*, 2:377–397, 2000.

[42] M.A Moffitt, C.C. McIntyre, and W.M. Grill. Prediction of myelinated nerve fiber stimulation thresholds: limitations of linear models. *Biomedical Engineering, IEEE Transactions on*, 51(2):229–236, 2004.

[43] C.A. Bossetti, M.J. Birdno, and W.M. Grill. Analysis of the quasi-static approximation for calculating potentials generated by neural stimulation. *Journal of Neural Engineering*, 5:44–53, 2008.

[44] S. Joucla, A. Gliere, and B. Yvert. Current approaches to model extracellular electrical neural microstimulation. *Frontiers in Computational Neuroscience*, 8(13), 2014.

[45] K.W. Altman and R. Plonsey. Analysis of excitable cell activation: relative effects of external electrical stimuli. *Medical & Biological Engineering & Computing*, 28(6):574 – 580, 1990.

[46] M. Solomonow. Comments, with reply, on "Point source nerve bundle stimulation: effects of fiber diameter and depth on simulated excitation" by K.W. Altman and R. Plonsey. *IEEE Transactions on Biomedical Engineering*, 38(4):390, 1991.

[47] B.J. Roth and J.P. Wikswo. Electrical stimulation of cardiac tissue: A bidomain model with active membrane properties. *IEEE Transactions on Biomedical Enginneering*, 41(3):232–240, 1994.

[48] H. Meffin and T. Kameneva. The electrotonic length constant: A theoretical estimate for neuroprosthetic electrical stimulation. *Biomedical Signal Processing and Control*, 6(2):105 – 111, 2011.

[49] K. Ogata. *Designing linear control systems with MATLAB*. Prentice Hall, 1994.